

1 Article

2 Experimental analysis of friction and wear of self- 3 lubricating composites used for dry lubrication of 4 ball bearing for space applications

5 Guillaume Colas ^{1,*}, Aurélien Saulot ², Yann Michel ³, Tobin Filleter ⁴, Andreas Merstallinger ⁵

6 ¹ Univ. Bourgogne Franche-Comté FEMTO-ST Institute CNRS/UFC/ENSMM/UTBM, Department of
7 Applied Mechanics, 24 rue de l'Épitaŕphe, F-25000 Besançon, France; guillaume.colas@femto-st.fr

8 ² Université de Lyon, LaMCoS, INSA-Lyon, CNRS UMR 5259, France; aurelien.saulot@insa-lyon.fr

9 ³ Centre National des Etudes Spatiales, 18 avenue Edouard Belin, 314001 Toulouse Cedex 9, France;
10 yann.michel@cnes.fr

11 ⁴ Department of Mechanical & Industrial Engineering, The University of Toronto, 5 King's College Road,
12 Toronto, ON, Canada, M5S 3G8; filleter@mie.utoronto.ca

13 ⁵ Aerospace & Advanced Composites GmbH, Viktor-Kaplan-Strasse 2, 2700 Wiener Neustadt, Austria,
14 Email: andreas.merstallinger@aac-research.at

15
16 * Correspondence: Guillaume.colas@femto-st.fr ;

17 Received: date; Accepted: date; Published: date

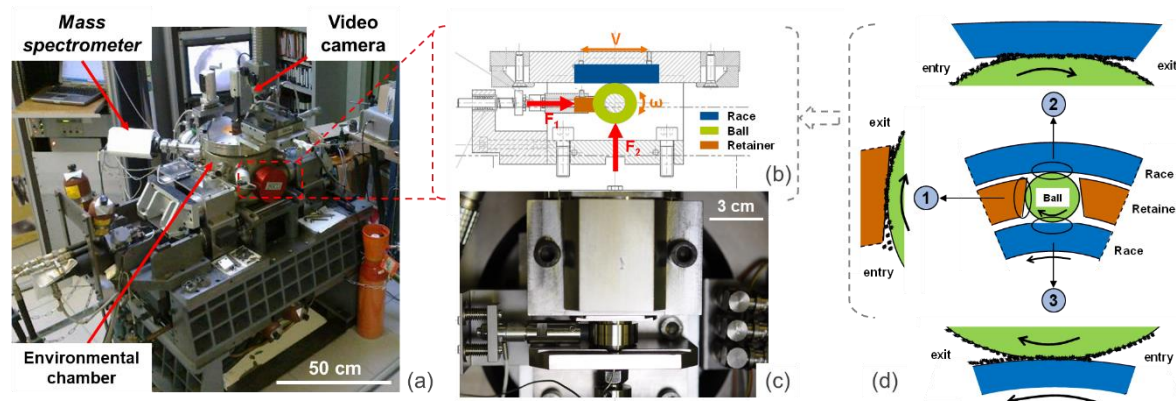
18 **Abstract:** Lubricating space mechanisms is a challenge. Lubrication must be sustained in different
19 environments, for very long period of time, and without any maintenance possible. This study
20 focuses on self-lubricating composite used in the double transfer lubrication of ball bearing.
21 Ball/races contacts are lubricated via transfer of materials from the cage that is made of the
22 composite. A dedicated tribometer has been designed for the study. A specificity of the tribometer
23 is to not fully constrain the composite sample to let it move as the cage would do in the bearing.
24 Four composites (PTFE, MoS₂, glass or mineral fibers) were tested in ultrahigh vacuum and humid
25 air environments. Transfer was achieved with morphologies and composition similar to what is
26 observed on real bearings. Adhesion measurements performed on composite materials before and
27 after friction allowed to explain the differences in tribological behaviors observed (transfer quality,
28 contact instabilities). Beyond strengthening the composites, fibers are shown to be critical in
29 trapping mechanically and chemically the transferred material to lubricate and prevent instabilities.
30 Equilibrium between internal cohesion of transferred material, and adhesion to counterparts must
31 be satisfied. Mass spectrometry showed that water appears also critical in the establishment of stable
32 transfer film, even in vacuum.

33 **Keywords:** composite; lubrication; friction; wear; adhesion; vacuum; ball bearing

35 1. Introduction

36 Lubricating space mechanisms is a difficult task as the mechanisms sees multiple environments
37 on the ground (UHV, humid air, dry nitrogen) and in space (low Earth orbit, deep space). Many
38 mechanisms are expected to last multiple years, leading to very long wear life of the tribological
39 components, up to hundreds of million rotations for a ball bearing [1,2]. In numbers of applications,
40 for example where bearings are operating in boundary condition, solid lubrication is preferred to
41 fluid and grease lubrication [2,3]. Coatings and composites materials are the solutions extensively
42 used, sometimes in combination [2,3]. This study is focusing on investigating the tribological
43 behavior of four self-lubricating polymer matrix composite materials, two commercially available
44 and two under development, used or intended to be used to lubricate ball bearing. A vast panel of

45 polymer-matrix composites materials have been developed to lubricate sliding contact [4–11]. Self-
 46 lubricating materials are well known to provide low friction and low wear in a wide range of sliding
 47 speed [7,11–13], temperatures [7,14,15], and humidity [7,8,16]. Related applications targeted in this
 48 study are spacecraft components whose service temperatures are in a low range within -55°C to +
 49 50°C [17]. Consequently, extreme temperatures such as those encountered in cryogenic applications
 50 are not of interest in this study. However, it has been shown that such composites can be successfully
 51 used in such cases [18].
 52



53

54 **Figure 1** - Double Transfer Test Bench (DTTB): (a) full tribometer; (b) cross section view of the DTTB;
 55 (c) top view of the contact between the cage and the ball; (d) schematic of the double transfer
 56 lubrication

57 The transfer lubrication (**Figure 1d**), also called double transfer lubrication, is an example of
 58 “useful wear” because the lubrication is made by a sacrificial cage material. Indeed, this lubrication
 59 process relies on the production of wear particles at the ball/cage interface by sliding motion [19–25].
 60 Particles are formed during sliding at the ball/cage contact interface (step 1). The particles, once
 61 formed, either fall on the inner race, or form a cluster at the exit of the contact. Minimal pressure of
 62 few MPa is sufficient to ensure cage wear [4]. Then (step 2), the particles adherent to the ball surface
 63 are transported to the ball/outer race due to the rolling motion of the ball on the race. They enter and
 64 circulate inside the contact to be crushed and compacted. As the ball keeps rolling, some particles are
 65 transferred to the outer race surface and form a layer on the surface, while others still adhere to the
 66 ball surface. At the end of step 2, particles and layers of compacted particles are formed on both the
 67 ball and the outer race. Eventually, at step 3 the same process takes place at the ball/inner race
 68 interface. It should be noted that the particles that have fallen on the inner race after being formed at
 69 the ball/cage interface during step 1 can enter inside the ball/inner race contact at step 3. At the end
 70 of step 3, particles and layers of compacted particles are formed on the inner race. Thus, there is an
 71 initial transfer of lubricating particles from the cage to the ball and a second transfer from the ball to
 72 the races.

73 Once the transfer films are formed, the wear rate of the cage must be almost null and any new
 74 particles formed must ensure the renewal of the films. Cage’s wear is critical to the success of the ball
 75 bearing lubrication but it must be kept low to maintain ball to pocket clearances throughout bearing
 76 lifetime [2]. In brief, successfully formulating composites requires controlling wear particle flows
 77 from the cage, their circulation and reuse, and the mechanisms by which they can form a transfer film
 78 and remain adherent to surfaces.

79 During decades Duroïd 5813 (PTFE matrix, glass fiber, MoS_2 particles) has been widely used as
 80 cage composite material. Following the cessation of the Duroïd 5813 manufacturing in the 1990s [3],
 81 PGM-HT has been identified by ESTL and ESA as the best candidate to replace it as the self-
 82 lubricating material for space application, providing some specific requirements on its fabrication
 83 and use [4,26,27]. However, discussions remain on its lubrication performances in ball bearings,
 84 especially on its capability to transfer material on both the balls and the races without damaging them
 85 to ensure good lubrication [1,28]. To avoid lubrication failure, it has been recommended to coat both

86 the balls and the races with MoS₂ [27]. However, in some cases it is primarily the coating that is
87 lubricating the contacts and not the composite [29].

88 Consequently, the uncertainties and limitations of the PGM-HT urge the development of new
89 material. On European side, numerous studies at ESTL, AAC, CNES and ESA mainly investigated
90 the materials on Pin-On-Disc (POD) or bearing testers [1,26,28,30] and compared the performances
91 of materials (friction coefficient and wear) depending on the nature of their constituents using PGM-
92 HT and Duroïd as references. From Pin-On-Disc to bearing a big gap exist due the differences in the
93 emulated kinematics. The literature [31–33] shows that the degrees of freedom of the system applying
94 the contact conditions have a big impact on the creation and the distribution of the 3rd body inside
95 the contact, which may leads to opposite results should the tests are conducted on different
96 tribometers, even if similar contact conditions are applied. The 3rd body is essentially composed of
97 the particles detached from the materials initially in contact (called 1st bodies) and circulating inside
98 the contact [34,35]. Here the 3rd body is eventually becoming the transfer films on both balls and races,
99 and it carries loads and accommodates velocity at the contact. The 3rd body has its own mechanical,
100 physical, and chemical properties which make it a different material as compared to the materials
101 initially in contact.

102 For this study, a dedicated Double Transfer Test Bench (DTTB) [36] to study more fundamentally
103 the double transfer mechanisms encountered in the dry lubrication of ball-bearing has been designed
104 and manufactured (**Figure 1**). This unique setup (further described in section 2) fully emulates the
105 cage/ball/race system through a two-contact configuration. It is able to tackle current limitations of
106 POD, and bearing testers in the study of transfer lubrication. The aim is to highlight more quantitative
107 criteria to test/validate and ideally design new materials.

108 The 2015 ESMATS communication reports the results of the 8 composites tested [36], here the
109 paper focuses on the 4 main one with extended morphological and chemical analysis of surfaces as
110 well as adhesion measurements to further explain the different tribological behaviors. Adhesion is
111 characterized at nanoscale using Atomic Force Microscope (AFM), but using cantilevers with
112 stainless steel microbeads fixed in-house on them. Consequently, the adhesion is probed directly with
113 the relevant tribological materials, such approach was only used on coating in a previous study
114 [29,37].

115 Consequently, the DTTB and the associated analysis will help to understand the 3rd body
116 creation, its circulation inside the contact and ultimately its arrangement to form the transfer film. In
117 other words, such unique global understanding approach will help understand the friction and wear
118 processes governing the double transfer lubrication, and consequently the associated tribological
119 behavior observed in space mechanisms.

120 2. Materials and Methods

121 2.1. Composite Materials

122 Four composite materials are studied. Among them, 2 reference materials: 1 that was
123 commercially available (Duroïd 5813) and widely used but whose production ceased decades ago,
124 and the now recommended composite that is commercially available (PGM-HT). **Table 1** gives
125 detailed information regarding the composites tested. AAC-C1 and AAC-C9 are the result of a
126 previous study during which several materials were tested on a common POD test configuration in
127 different environments to identify the most promising formulation [5]. For those 2 composites,
128 dimensions of both the fibers (in diameter) and the MoS₂ particles lie between those of Duroïd 5813
129 and PGM-HT. To our knowledge, in AAC-C1, AAC-C9, and PGM-HT, fibers are dispersed in the
130 matrix with random orientations in accordance with decades old recommendations [20]. Duroïd 5813
131 differs in that it is a bidirectional composite with 2/3 of the fibers oriented in one direction, 1/3 in the
132 orthogonal direction, none oriented along the third direction [12]. PGM-HT exist with different pre-
133 conditioning and the tested PGM-HT is preconditioned in vacuum at 240°C for 24h as recommended
134 by ESA in 2012 [4,27].

135
136**Table 1** - Composites designation, compositions, and mechanical properties. * measured through X-ray tomography [38]

Composite	Supplier	Composition	Manufacturing Process	Young's modulus (GPa)
Duroïd 5813	Rogers Corp. (USA)	PTFE matrix ~18% MoS ₂ Ø10µm * ~19% glass fiber Ø3µm *	unknown	6.1 [39]
PGM-HT	JPM Mississippi (USA)	PTFE matrix ~10% MoS ₂ Ø100µm * ~24% glass fiber Ø20µm *	Hot compression molding pre-conditioned in vacuum	1.1 [39]
AAC-C1	formulation by AAC, produced by ENSINGER SINTIMID GmbH	PTFE matrix 10% MoS ₂ particles 25% glass fiber Ø13µm	Hot compression molding	-
AAC-C9	formulation by AAC, produced by ENSINGER SINTIMID GmbH	PTFE 10% MoS ₂ particles 15% mineral fiber Ø3µm	Hot compression molding	-

137

138 *2.2. Friction tests*139 *2.2.1. The Double Transfer Test Bench (DTTB)*

140 The Double Transfer Test Bench (DTTB) (Figure 1), specifically designed and manufactured for
141 the study, can simulate both cage/ball and ball/race contacts at once. It operates in a fully equipped
142 environmental chamber. As shown on **Figure 1**, the bearing is simulated with 3 samples:

- 143 • A barrel shaped roller (Ø 25mm, roundness Ø 1000mm) whose motion is only rotation.
144 A drawing of the specimen is given in supplementary information (SI),
- 145 • A plate sample (l = 109mm, w = 10mm, t = 14mm) whose motion is only translation,
- 146 • A pad sample (Ø 8mm) made of the composite to be tested to emulate the cage.

147 The motion control of the roller and the plate is done via PID feedback loop in a master/slave
148 configuration, the master being the ball. It allows performing both pure rolling and rolling with
149 sliding kinematics. Normal and tangential forces between the roller and the plate are measured
150 through a XYZ piezoelectric sensor on which the motor is rigidly fixed. The plate sample is mounted
151 on a structure moving in x direction. Both the roller (motor) and the composite pad are mounted on
152 the same bottom plate that moves vertically to make contact between the roller and the plate, and
153 apply F₂. The roller can be in contact with the composite pad only or with both the composite pad
154 and the plate. The composite pad is mounted on a sensor measuring the force F₁ with a sensitivity of
155 ±0.01 N. The sensor allows monitoring the variations of the load all along the test. The contact load
156 F₁ between the sample simulating the cage and the ball, is applied via two compression springs. The
157 assembly is guided in the support thanks to two roller guides. As it is shown in Figure 1, the assembly
158 is a long-suspended structure that gives the freedom to its end (basically the surface in contact with
159 the ball) to slightly move around its center position. Such freedom was chosen as the contact between
160 the ball and the cage in a bearing is far from being rigidly fixed.

161 The ball and plate samples are made of AISI440C with a roughness Ra < 0.1 µm. Prior to
162 experiments, samples are cleaned with respect to a protocol recommended by CNES [40]. Composite
163 samples are machined with respect to the machining process of the real bearing cages to get a similar
164 surface finish of the socket surface. Finally, no MoS₂ coatings are deposited on samples in order to
165 study only the capability of the materials to double transfer on the ball and on the race.

166 2.2.2. Contact conditions

167 The kinematic is an alternative motion. The displacement amplitude of the plate sample is 75
 168 mm in total which covers approximately 95% of the roller perimeter. Therefore, there is no
 169 overlapping of the track ends. The linear speed of the ball is 100mm/s and representative of space
 170 mechanisms' bearings, such as those used in the STD and Polder [1]. It is also the sliding speed used
 171 to pre-select the composites C1 and C9 in [30], and to test other composite compositions [4].

172 Contact loads are 1.5 N at the contact pad/roller (around 10 MPa of max Hertz theoretical initial
 173 contact pressure) and 125 N at the contact roller/race (0.5 GPa of max Hertz contact pressure).
 174 Experiments are conducted in UHV (10^{-7} mbar) and in air 50%RH (Relative Humidity). Experiments
 175 are done in 3 phases of 5000 cycles each to emulate different working conditions:

176 A - Running in with only the roller/composite pad contact to emulate the gentle run in

177 B - Rolling without sliding with both roller/composite pad and roller/plate contacts

178 C - Rolling with 0.5% sliding with both contacts to emulate severe working conditions

179 One cycle gathers both the back and forth motions. All 3 phases are not performed during each
 180 test. That allows to better study the friction and wear behavior of the materials in contact. To
 181 understand what happens at each step, some materials can see only the phase A or the phases A & B.
 182 Experiments containing only phase A allow top view visualization of the ball. Procurement of
 183 materials has been difficult for PGM-HT and Duroid 5813 samples with only very limited quantity.
 184 Phases A & B allowed for reproducibility assessment of the tests. Consequently, a video camera is
 185 used to study the friction track on the ball.

186 2.2.3. Real time and Post tribological tests analysis

187 A quadrupole mass spectrometer (QMS 200, Pfeiffer Vacuum) is used to continuously monitor
 188 the composition of the vacuum environment and the adsorption/desorption triggered by friction.
 189 Such monitoring allows tracking the degradation of the materials in contact during a friction test,
 190 determining which of the material is mostly stressed, and detecting if molecules from the vacuum
 191 environment are used by the contact [41–45]. Focus is on the masses relevant to the degradation and
 192 wear of PTFE, stainless steel, and MoS₂ [45–48]. Interest is also given to gaseous species known to
 193 affect the tribological behavior of the different constitutive elements of the composites (water,
 194 oxygen, carbon monoxide and dioxide, nitrogen). Numerous atomic masses are taken into
 195 consideration for each gas molecules of interest (**Table 2**). Molecules are fragmented during the
 196 measurement process. The relative abundance of each fragment as compared to the main one allows
 197 determining which molecule is detected. As can be seen in **Table 2** one atomic mass can be
 198 representative of multiple molecules.

199 **Table 2** - Gas molecules of interest and the associated atomic masses in the gas analysis conducted by
 200 mass spectrometry analysis [49]. It was chosen to present hydrocarbon molecules as C_xH_y molecules
 201 because the resolution of the mass spectrometer vs. the measurement speed is not high enough to
 202 confidently dissociate different hydrocarbons.

Molecules	Corresponding atomic masses	Molecules	Corresponding atomic masses
H ₂ O	18, 17, 16, 1	H ₂	2, 1
O ₂	32, 16	F	19
CO	28, 16, 12	HF	20
CO ₂	44, 28, 22, 16, 12	CF ₄	70, 69, 45, 31, 19
N ₂	28, 14	C ₂ F ₄	100, 81, 69, 50, 31, 29, 19, 12
H ₂ S	34, 33, 32	C ₂ F ₆	(119), 69, 50, 31, 29, 19
SO ₂	64, 48, 32, 16	C _x H _y	46, 45, 44, 43, 42, 41, 39, 31, 30, 29, 28, 27, 26, 19, 16, 15, 12, 1
Ar	40, 20		

204 For test in which only phase A is performed, live video of the test is recorded to monitor the
 205 transfer of composite material from the pad to the roller. High-definition video (1920 × 1200) is
 206 recorded thanks to a Nikon D5000 camera whose shutter is maintained open to get a continuous live
 207 view recording on the computer via USB3 connection.

208 Post-test morphological and chemical analysis are performed. Keyence VHX-2000 digital optical
 209 microscope is used to study the morphology of the friction tracks. Eventually, detailed morphological
 210 analyses of the friction tracks are conducted under Scanning Electron Microscopy (SEM) (FEI Quanta
 211 600) in low partial pressure mode (130 Pa) to not melt the composite material and avoid charging.
 212 Chemical elemental analyses are also conducted using Energy Dispersive Spectroscopy (EDS)
 213 (Oxford Instrument) analysis.

214 2.3. Adesion measurements

215 Adhesion measurements were conducted on an Asylum Research MFP-3D AFM mounted on
 216 active damping system to filter out vibration coming from the building. The whole [AFM + active
 217 damping system] is installed in an acoustic chamber to isolate it from the room and associated noise.

218 **Table 3** - Parameters used in the adhesion forces measurement. * Beaded cantilevers with borosilicate
 219 bead are commercially available, AISI 440C bead are glued in-house on tipless cantilevers and are
 220 measured. The closest to 20µm in diameter was chosen for the study.

Parameter	Value
Loading Pattern (µN)	1, 2, 3, 2, 1
Measures at each load	6
Approach speed (µm/s)	1.98
Dwell time (s)	1
Environment	Humid air (50%RH)
Temperature	Room temperature (~25°C)
Beads materials and diameter*	Borosilicate (Ø20µm) AISI440C (Ø19.5µm)
Studied composites	C1 after Ion Milling C1 after friction: center and periphery of the track PGM-HT after Ion Milling PGM-HT after friction: center and periphery of the track Pure PTFE for reference

221 Parameters used in the adhesion measurement are presented in **Table 3**. Measurements are
 222 conducted in humid air (50%RH) at room temperature (~25°C). All measurements are done using the
 223 same approach and retract speeds, and dwell time (time during which the bead stays in contact with
 224 the surface at the defined load). Multiple loading forces are used following a defined loading pattern
 225 (**Table 3**). Loading is repeated 6 times in row at each load, which leads to 6 adhesion force values at
 226 each load. Six repetitions are performed to make sure 5 data points per load can be considered. On
 227 each sample, adhesion forces are measured using the same implemented procedure:

229 1. High resolution image of the 70×70 µm² region of interest ROI. Prior to full adhesion
 230 measurement and make sure the ROI are gathering the 3 main constitutive elements of
 231 the composites (glass fiber, MoS₂ particles, and PTFE matrix), and 3rd body particles (for
 232 samples that underwent friction). NanoWorld AG NCHR sharp tip Si cantilevers (42
 233 N/m stiffness) were used for high-resolution imaging of regions of interest. Using high
 234 resolution images allows for confident surface pattern recognition after scanning with
 235 the Ø 20 µm beads prior adhesion measurement. Images appears blurrier which can

- 236 mislead the localization of the constitutive elements. SEM images of those ROI are also
 237 used to fully grasp their morphologies and link them to adhesion.
- 238 2. Mounting of the beaded cantilever and stabilization of the environment. Cantilever is
 239 approached towards the surface, put in contact and then retracted just above the surface
 240 to make sure the system reached both an equilibrium temperature and the required
 241 humidity prior doing measurements.
 - 242 3. Tapping mode image of the ROI with the beaded cantilever

243
 244 Adhesion measurements: 3 to 6 locations of measurement are selected on each constitutive
 245 elements of the composite, which leads to 9 to 18 locations on a single ROI. They are selected far
 246 enough from the borders of each components to avoid disturbances on the measures. Selected
 247 locations are randomly distributed and chosen between all components to make sure any transfer of
 248 material from one component to the bead can be detected. Such transfer to the probe might impede
 249 the subsequent measures and must be avoid. Eventually, adhesion measurements are performed
 250 twice on the first location, at the beginning and at the end of the round of measurement, to check if
 251 adhesion changed, which would indicate changes on the bead surface.

252 Composites studied in this section are PGM-HT and AAC-C1 composite pads after complete test
 253 (phases A, B, C) in UHV. C9 and Duroïd 5813 have fibers that are thin and dispersed everywhere,
 254 but that can also be found as bundles. The bead was too large to confidently characterize the adhesion
 255 with one single element. Due to the roughness of the samples, smaller bead made it impossible to
 256 image the surface because the cantilever was repeatedly hitting walls. That led to cantilever breakage
 257 or bead removal.

258 The objective of the adhesion measurement is to characterize the adhesion between the
 259 composite materials with the sliding/rolling counterparts, and to characterize as much as possible the
 260 adhesion between composite internal components when fragments are created during friction. The
 261 selected materials are AISI440C and borosilicate. Ideally, glass fiber fragments should have been used
 262 but geometries were too erratic, borosilicate composition is similar to the glass fiber except for the
 263 sizing that is not known. However, under friction, fragments are created and overall exposed bulk
 264 fiber surface becomes greater than the sizing covered surfaces. **Table 4** presents the interfaces whose
 265 adhesion has been characterized experimentally during the study.

266 **Table 4** - interface whose adhesion is characterized experimentally during the study.

Composite	PTFE	Glass Fiber	MoS2	3 rd body
PTFE	-	☑	-	-
Glass Fiber	☑	☑	☑	☑
MoS2	-	☑	-	-
3 rd body	-	☑	-	-
AISI440C	☑	☑	☑	☑

267
 268 As mentioned previously, adhesion measurement was performed using beaded cantilevers.
 269 Tipless NANOSensorSTM TL-NCH cantilevers (42 N/m stiffness) modified in-house with Ø 20 mm
 270 AISI 440C stainless steel beads (Sandvik Osprey Ltd) were used for adhesion measurements. The
 271 AISI 440C beads were cleaned of contaminants using a Branson1 M1800H ultrasonic cleaner in
 272 acetone and ethanol for 5 min each, and then dried in an oven (Cole-Parmer1 Model 281A) for 30 min
 273 at 45±5 °C. They were glued to the cantilevers using PC-Super Epoxy. To remove any contamination
 274 covering the interacting surface of the bead, the cantilevers were submerged in acetone for 1 min,
 275 then in ethanol for 1 min to wash away the acetone and any other residues.

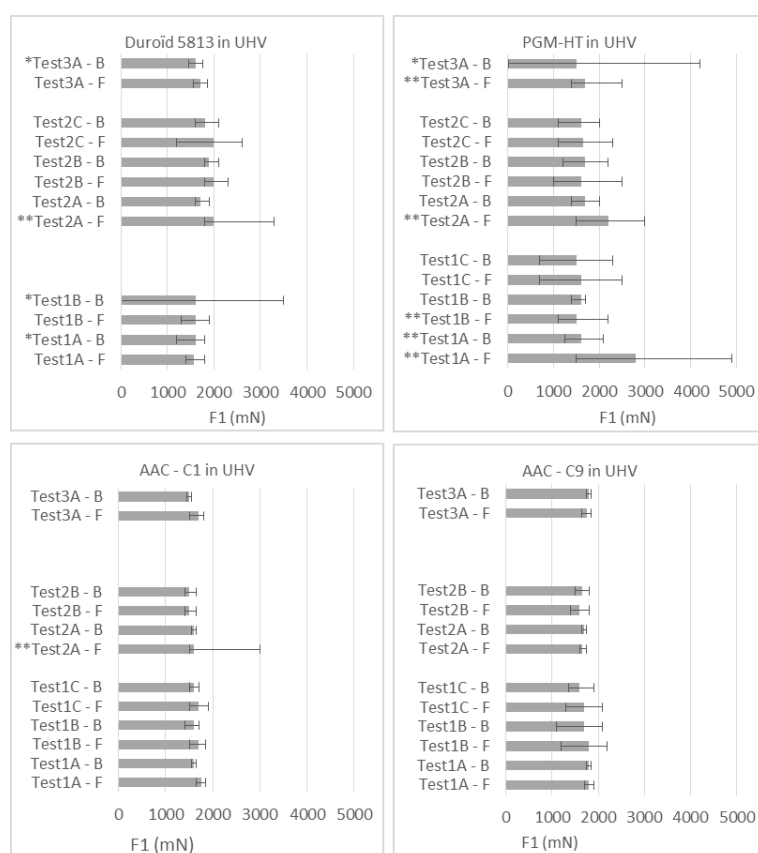
276 Considering the limitation of AFM measurements towards the sample roughness, adhesion
 277 measurements have been done on both original bulk material to have reference values of adhesion
 278 prior to friction, and to compare the results with adhesion measured after friction. The friction track

279 on the composite pad exhibits an elliptic shape surrounded by a contour comprised of particles and
 280 debris that have been ejected outside the contact. Adhesion is measured in the center of the ellipse
 281 and in the periphery where the center meets the contour. The reference samples were prepared by
 282 Ion Milling (IM) using a Hitachi IM400-Plus and Ar gas. Adhesion measurements on the IM prepared
 283 samples were done immediately after milling to minimize surface contamination and related impact
 284 on adhesion forces.

285 3. Results and discussion

286 The results will focus on the variations of the normal load F1 at the contact between the
 287 composite pad and the roller, the mass spectrometry (only for UHV tests), and on the post-test
 288 analyses. F1 is the only force discriminating the different composites as explained in appendix A. The
 289 significant events such as big particle detachment or circulation inside the contact can be clearly
 290 detected on F1 thanks to the degrees of freedom intentionally given to the pad (cf. **Figure 2** and
 291 section 3.1.1). Instabilities inside the roller/pad contact are also observable on F1 due to the activation
 292 of a resonance frequency of the system. It is believed that the combination of suspended assembly
 293 and the springs greatly amplifies the magnitude of displacement, hence allowing detection of those
 294 instability events during the friction life of the contact. Changes in the transfer film properties and
 295 composition, even in two contact configurations, directly affect the behavior of the roller/pad contact.
 296 Consequently, F1 efficiently helps to discriminate the materials and link their behavior to both the
 297 composite, the friction tracks, and 3rd body compositions and morphologies. Those are studied with
 298 SEM and EDS after the test. The evaluation of both the transfer capabilities of materials and the 3rd
 299 body morphology is qualitative.

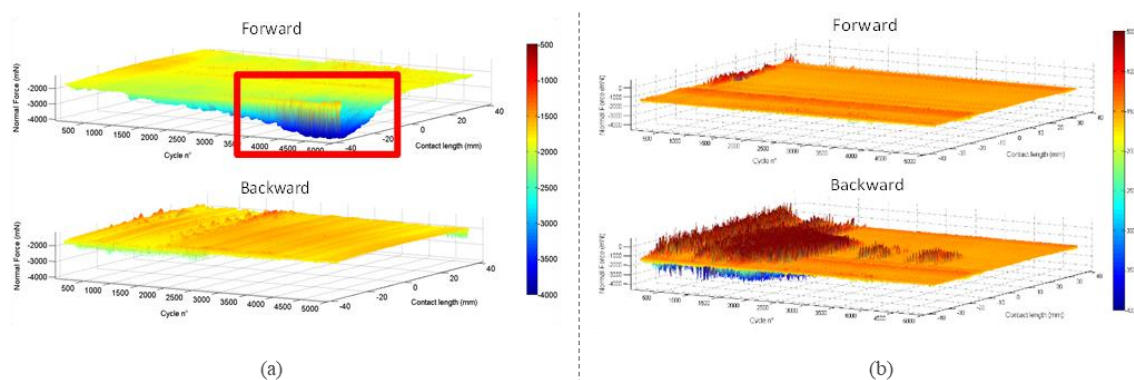
300 3.1. Tests in UHV environment



301

302 **Figure 2** - Variation of normal force F1 at the contact between the composite pad and the roller. B and
 303 F refers to Backward and Forward motion of the alternative sliding direction. Errors bars represent

304 the min/max amplitude of F1 during the test. * refers to high min/max variations originating from
 305 noise, and ** originating from big particles circulation inside the contact.



306
 307 **Figure 3** - Force F1 as a function of track length and cycle number from Duroïd 5813 during (a) test2A,
 308 and (b) test1B. Red square shows how significant the effect of particle circulation can be on F1. Note
 309 that force values are negative because the sensor is in compression.

310 3.1.1. Friction force

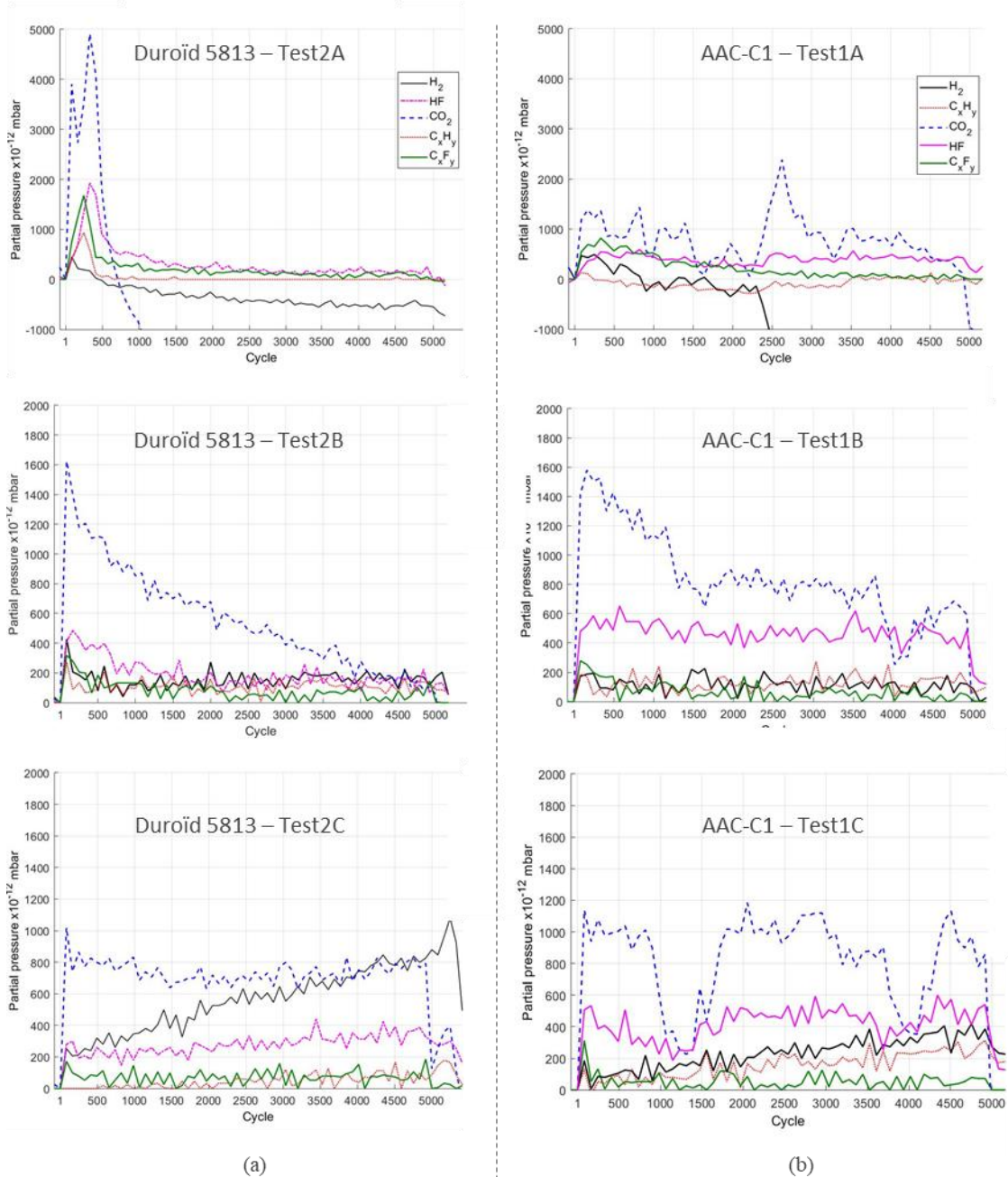
311 **Figure 2** displays the mean friction force F1, and its mean and max values measured as depicted
 312 in Appendix A. AAC-C1 displays the most stable F1 force, except for the significantly high maximum
 313 force during Test2A-F due to the circulation of the 3rd body particles inside the contact, which pushes
 314 the pad backward leading to an increase of the force magnitude. Such big particle circulation is also
 315 detected with Duroïd 5813 (**Figure 3a**) and PGM-HT. All significant occurrences are in phase A of the
 316 tests, which makes sense as all particles are squeezed when entering the roller/plate contact in phases
 317 B and C. Nonetheless, such big particle circulation is occurring more often with PGM-HT. PGM-HT
 318 is also the composite that exhibits the greatest variations in F1. Such medium high amplitudes of
 319 variations might be the result of 3rd body particles hard enough not to be completely flattened in the
 320 roller/plate contact, and consequently large enough to be detected by the force measurement. All 3D
 321 representations of F1 as a function of cycle number and track length can be found in supplementary
 322 information SI.2.

323 Overall, PGM-HT performs the worst and exhibits the highest range of variation around the
 324 mean values. Multiple event of big particle generation happened in phase A for all tests, which may
 325 explain the high variations observed in phases B and C. Duroïd 5813 exhibits a rather stable (low
 326 variation) but sporadically noisy behavior. Instabilities are indeed observed with Duroïd 5813, mostly
 327 during Test1B-B, but only during a limited period of time and over a portion of the track length
 328 (**Figure 3b** and SI.1). It might be that a run-in was needed to stabilize the interface and the transfer
 329 film on the roller to bring the F1 back to almost constant without significant fluctuations. AAC-C9
 330 composite exhibits a very similar behavior to AAC-C1, it is also closer to Duroïd 5813 from F1
 331 variations. Instabilities are almost inexistent with both AAC-C1 and AAC-C9. Except for Test2 A-F
 332 where big particle detachment is detected, variation of F1 around the mean value is lower than what
 333 is observed for AAC-C9, particularly when stresses increase at the roller/plate contact (phases B and
 334 C). Consequently, under vacuum, the composite AAC-C1 is the best candidate among the four
 335 composites studied here.

336 3.1.2. Mass spectrometry

337 **Figure 4** displays typical mass spectra obtained during the friction tests and it is mainly showing
 338 the degradation of the composite material. For the sake of clarity, and to highlight levels of the friction
 339 induced desorption, all offsets are removed. Focus is on F based molecules (HF, C_xF_y) which can be
 340 related to the PTFE matrix of the composite [48], on both hydrocarbons (C_xH_y) and CO₂ that can be
 341 related to MoS₂ [45,50], and on H₂ which is a typical desorption product of stainless steel under
 342 tribological stress [46,50,51]. H₂ desorption can also be related to MoS₂ to a lower extent [50,52]. Water

343 desorption is not shown because it is observed on all composite and without any specific trends in
 344 its variation, except for AAC-C1 in phase A. In the latter case, spectra including water are presented
 345 in SI.5, they show adsorption of water during friction in phase A. In all other cases, it appears that
 346 the water trapped inside the composite material is being continuously desorbed during friction.
 347 **Figure 4** displays mass spectra obtained with Duroïd 5813 and AAC-C1 composites, mass spectra
 348 from PGM-HT and AAC-C9 can be found in supplementary material SI.4.



349

350 **Figure 4** - Typical mass spectra obtained during friction tests with Duroïd 5813 (a) and AAC-C1 (b)
 351 composite materials.

352 Duroïd 5813 and PGM-HT show similar behavior. The desorption of F containing ions directly
 353 demonstrates that they are both consumed/solicited for a defined period of time during phases A and
 354 B. Note that during phase A, PGM-HT degradation, in terms of desorption, is barely detected (SI.4).
 355 To the contrary, Duroïd is significantly stressed during the first 1000 cycles in phase A, and during
 356 the first 2000 cycles in phase B, as degradation is detected. Similar trend is observed for PGM-HT
 357 in phase B (SI.4). However, for PGM-HT, there is a large peak of H₂ desorption during the first cycles of

358 phase B, which may be linked to the stainless steel undergoing significant stress [46,51]. That is a
359 reasonable assumption as the absence of degradation of the composite in phase A may be related to
360 ineffective transfer, and consequently related to absence of lubrication of the roller/plate contact. It
361 also supports well the observation of debris comprised of steel in ball bearings solely lubricated by
362 PGM-HT [1]. In Phase C, both composites appear to be degraded/stressed throughout the entire test
363 duration. This might be related to the need of a higher quantity of transferred material to properly
364 lubricate the roller/plate contact that is under the severe rolling+sliding condition.

365 Composites C1 and C9, on the other hand, demonstrate degradation/stress of the composite
366 throughout the entire test duration for all phases A, B, and C (**Figure 4** and SI.5). The partial pressure
367 elevation detected in the chamber by the mass spectrometer is 2 to 3 times lower for C1 as compared
368 to C9. However, the friction induced desorption of C1 is within the same range as compared to
369 Duroïd 5813, while C9 show desorption levels close to that observed for PGM-HT. This is somewhat
370 counter intuitive as C1 composition is closer to PGM-HT and C9 composition is closer to Duroïd.
371 However, AAC-C1 adsorbs water during friction (SI.5), which may contribute to increased friction
372 stability thanks to the creation of carboxylate groups on PTFE to anchor the transfer film on the steel
373 surface [16].

374 Regarding the variations of the CO₂ desorption levels, it is interesting to note that they are
375 following the trends of C_xH_y and C_xF_y for Duroïd, and for AAC-C1 but only in phase C. For AAC-C1
376 it indeed appears that there are different sequences in desorption, such variation could be an image
377 of phases of 3rd body production to create and/or refill the transfer films to ensure lubrication. Over
378 the 3 phases, CO₂ desorption drops much faster with Duroïd than with AAC-C1. Similar observation
379 can be made with AAC-C9 as compared to AAC-C1, while PGM-HT is closer to Duroïd 5813. It can
380 consequently be assumed that MoS₂ is continuously and constantly stressed during friction. CO₂ is
381 known to be a common contaminant of MoS₂ [45,53], its desorption under friction can therefore be
382 linked to MoS₂ being stressed. If MoS₂ is more stressed, it may consequently create a more lubricious
383 transfer film, which in turn would explain why F1 is more stable with both AAC-C1 and AAC-C9 as
384 compared to both Duroïd and PGM-HT (**Figure 2**), particularly in phases B and C. This is in line with
385 Khedkar [11] that reports that MoS₂ is very effective in improving wear resistance of composites in
386 the presence of glass fibers as strengthening phase. H₂ desorption levels are approximately the same
387 for all composite in phases A and B, except for PGM-HT that is exhibiting a peak during the first 200
388 cycles. In phase C, H₂ is more desorbed with Duroïd than it is with AAC-C1, AAC-C9, and PGM-HT.
389 Trends of H₂ desorption is mostly following desorption trends of C_xH_y and C_xF_y, which may link it to
390 the composite rather than to the stainless steels, except for PGM-HT at the beginning of phase B.
391 However, another assumption could be that the steel surface needs to be activated to enhance the
392 transfer of material to the roller and plate surfaces and allow lubricious layer build up.

393 At this stage, post-test analyses of the surfaces are required to state on the wear level of the
394 material.

395 3.1.3. Surface analysis

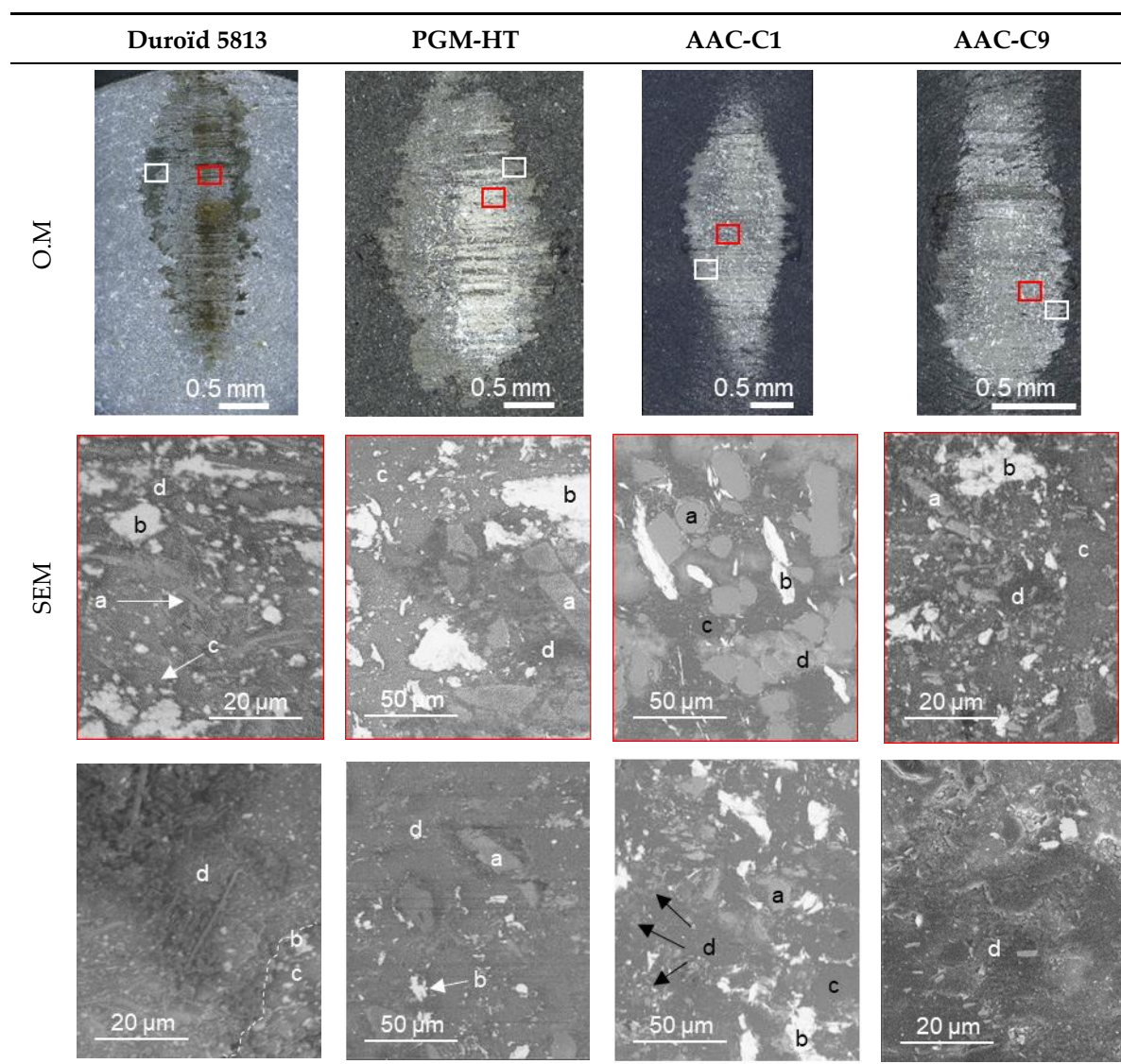
396 **Table 5** and **Table 6** show overall images of the contact ellipse on the self-lubricating pad and
397 the raceway on the flat specimen after a complete test, i.e. after the 3 phases A, B and C. The roller is
398 not shown because the track has the same appearance and morphology as the raceway on the plate
399 specimen. Optical images of the roller surface after running phase A of the test are shown in SI.4.

400 The two tables show that double transfer is effective with all materials. However, the qualitative
401 evaluation of the transfer shows that:

402 - PGM-HT transfers very little in phase A but produces some large clusters (SI.4). It transfers
403 very moderately in phase B as well. In phase C, the transfer is active but remains relatively low while
404 particle production remains average. That agrees well with the MS measurements (SI.5) which shows
405 no desorption during phase A, desorption of PTFE and MoS₂ related molecules during a short period
406 of time in phase B, desorption of the same species during all phase C. Note that in phase B there is a
407 peak of H₂ prior to C_xF_y, HF, and CO₂ desorption. That could be related to stainless steel stress and
408 activation of surface to initiate transfer as hypothesized earlier. At the end of the 3 phases, PGM-HT

409 transferred very little but produced a rather large number of particles which are mainly ejected near
 410 the contact ellipse on the pad. The layer of transferred 3rd body on the roller and the plate is comprised
 411 of a very thin and almost transparent layer with relatively large but homogeneously distributed
 412 clusters on top of it. Production of large particles forming clusters agrees well with the variations
 413 observed in F1.

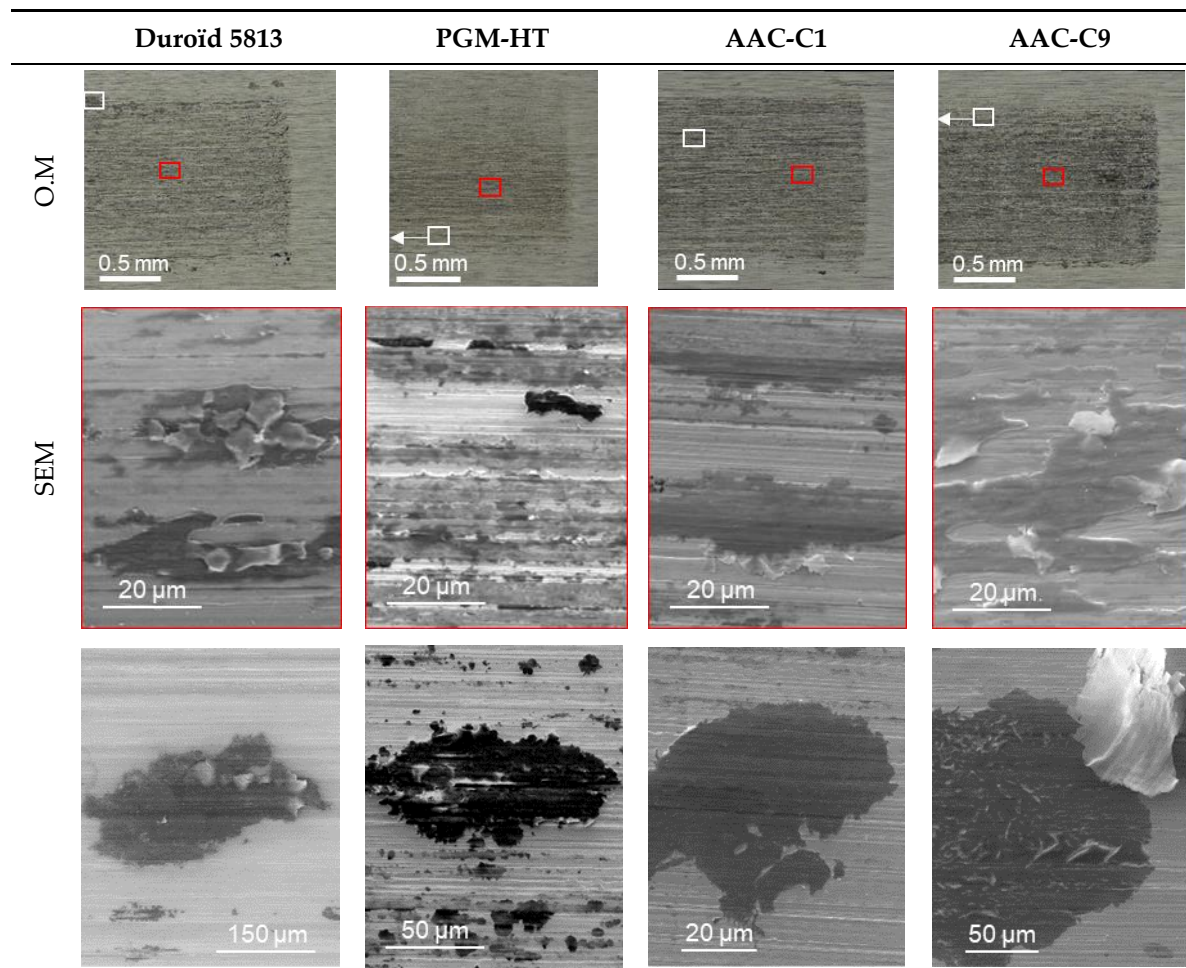
414 **Table 5** - Optical images of the contact area on the composite pad and detailed SEM images of the
 415 surfaces. a - fiber; b - MoS₂ particle; c - PTFE matrix; d: third body. Zoomed in image of the white
 416 framed region of Duroïd shows the sharp transition (dotted line) between friction track and debris.



417 - Duroïd, like PGM-HT, transfers very little in phase A (SI.3). However, it produces few particles,
 418 at least of large size (i.e. detectable on F1 measurement). In phase B, the transfer and production of
 419 particles detectable in the F1 measurement remains low. It is in phase C that the transfer is
 420 significantly activated. That agrees well with MS measurements, in phase A desorption of PTFE and
 421 MoS₂ related molecules is seen during a short period of time. Note that there is no peak of H₂
 422 desorption meaning that surface needs less activation to initiate particle detachment and transfer
 423 from the composite to the steel surface. In phase B, desorption is higher and lasts longer, which is in
 424 line with better transfer, and desorption occurs during all phase C. At the end of the 3 phases, the
 425 transfer is correctly carried out, the transferred material, although forming "patches" (smaller than
 426 those formed with PGM-HT) and smoother areas, is homogeneously distributed. A few particles can
 427 be discerned around the racetrack as well as in and around the ellipse. The 3rd body patches
 428

429 demonstrates elevated parts (SEM images in **Table 6**) as if it sticks to the counter surface which brings
 430 them up. A sticky 3rd body could explain instabilities observed on F1 (SI.1 and **Figure 2**) via stick-slip
 431 phenomenon. In total, the volume of particles appears to be smaller than that produced by PGM-HT.

432 **Table 6** - Optical images of the friction track on the plate sample and detailed SEM images of the
 433 surfaces.



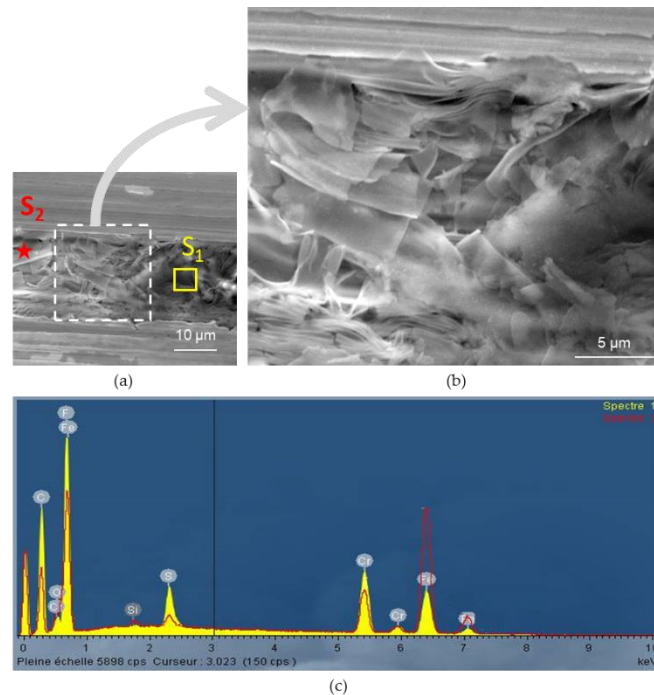
434 - AAC-C1 transfers more than Duroïd in all phases and produces significantly fewer particles
 435 (much less ejection around the contact ellipse and the raceway). It is important to note that unlike
 436 Duroïd 5813, PGM-HT, and AAC-C9, AAC-C1 transfers significantly in phase A, the transfer film on
 437 the roller is visible at naked eyes (**SI**). Such observation agrees well with the MS measurements that
 438 shows equal level desorption of PTFE and MoS₂ related molecules over the entire durations of the 3
 439 phases A, B, and C. H₂ is not significantly desorbed, which is in line with no specific damage of the
 440 steel, and that consequently confirm the capability of the composite to transfer efficiently low volume
 441 of material and provide stable friction (cf. F1 variations in SI.1 and **Figure 2**). The distribution of the
 442 material transferred to the raceway on the plane appears homogeneous. No elevated parts of patches
 443 are observed, contrary to Duroïd 5813. That could mean lower stickiness, which is in line with the
 444 absence of instabilities in F1. That shows that even during smooth run-in, lubrication can be effective
 445 very quickly.

447 - AAC-C9 appears to have transferred more than C1 when the test includes all phases A, B, and
 448 C. It is interesting to note that C9 transfers very little in phase A, but it produces a larger volume of
 449 particles. This goes against what could be expected considering the high level of desorption as
 450 compared to AAC-C1 which transfers material in phase A. Consequently, high desorption does not
 451 univocally mean high transfer but only high degradation. In phase B, AAC-C9 transfers moderately,
 452 then it transfers more in phase C. Overall, the transfer capability of AAC-C9 is very similar to PGM-

453 HT. Nonetheless, at the end of phase C, the transferred material seems to have a homogeneous
 454 distribution on the raceway but is thicker than what is observed with the other 3 composites. The
 455 volume of particles ejected in the vicinity of the contact ellipse on the pad is close to what is observed
 456 with Duroïd 5813.

457 All four composites considered, a significant volume of 3rd body particles remain trapped in the
 458 contact ellipse where friction takes place. Fibers are playing an important role in the trapping,
 459 especially the large fibers comprising PGM-HT and AAC-C1 composites. Indeed, a layer of powdery
 460 3rd body is surrounding the fiber and appears to isolate it from the rest of the matrix. This clustering
 461 of particle around the fibers could be enhanced by the opening of the interface due to delamination
 462 resulting from friction [12], the corner edge phenomenon observed with bi-phasic composites
 463 materials [54]. Both may lead to breakage of the fibers and the creation of fiber-based particles. Here,
 464 fibers however appear to be strongly bounded to the matrix as fibers are cleaved or abraded during
 465 friction without completely removing them from the matrix. Glass fibers have indeed been shown to
 466 poorly resist abrasion during sliding of PTFE composites as reported by Khedkar [11]. The layer of
 467 particles surrounding the fibers in the contact ellipse may also acts as a “buffer layer” to help
 468 accommodate stresses around the fibers and limit abrasion of the counter surface by the glass fibers.
 469 Nonetheless, PGM-HT exhibit a larger amount of fibers aligned parallel to the sliding direction. Such
 470 alignment has been shown to be detrimental and increase wear [12], which may explain why PGM-
 471 HT large particle creation and circulation inside the contact. AAC-C1 also exhibit some fibers aligned
 472 parallel to the sliding direction but, the reaction with water may mitigate the risk of wear thanks to
 473 better PTFE and MoS₂ transfer.

474 MoS₂ particles initially incorporated in the composite also appear to be strongly bounded to the
 475 matrix, as only few and small fragments are detected in the 3rd body. The 3rd body in the pad contact
 476 ellipse is mostly powdery and is a mixture of PTFE, MoS₂ and fiber fragments (glass for PGM-HT,
 477 Duroïd 5813, and C1, mineral for C9). In some places in the contact ellipse, the 3rd body forms a
 478 compacted patch of material, but such patches appear marginal as compared to the powdery one.
 479 However, those compacted patches exhibit a morphology similar to the morphology of the
 480 transferred materials on the roller and the plate.
 481



482

483 **Figure 5** - SEM images of the un-compacted 3rd body trapped inside scars in the friction track on the
 484 plate (a) and a zoomed-in image showing it layered structure in more details (b). EDS analysis of the
 485 3rd body, spectrum S₂ is conducted over the identified square area (c) AAC-C1 Test1 after test, end of
 486 phase C.

487 The 3rd body transferred to the plate mostly exhibits a compacted and ductile morphology (Table
 488 6). Some particles (powdery 3rd body) can also be detected but only sporadically, big patches are
 489 frequent and the edge of the friction track. Those patches are 3 to 6 times bigger than those
 490 encountered in the friction track. Small particles are seen in the transferred films. They are believed
 491 to be fiber and MoS₂ small particles (cf. EDS analysis of 3rd body agglomerate in SI.5). One specific
 492 feature was observed in the transferred film originating from AAC-C1, it is the stacking a lamellar
 493 material (Figure 5). Small particles can be seen inside each lamella (Figure 5b), similarly to what is
 494 observed in all transferred films. The EDS analysis demonstrate that the specific layered material
 495 created from AAC-C1 is mostly comprised of PTFE and MoS₂ particles as evidenced by C, F and S
 496 detection. Cr and Fe are fairly detected, this is the contribution of the steel substrate to the analysis
 497 because the transferred film is thin and the electrons goes through it revealing the steel. Si small
 498 detection can be both due to the steel contribution and the presence of tiny fiber fragments. Those
 499 extremely small fragments may help strengthen the film and help reducing wear similarly to the
 500 Al₂O₃ nanoparticles from the PTFE/Al₂O₃ composites [6], and hard fillers [10]. Furthermore, SiO₂ has
 501 been shown to be a beneficial filler to significantly decrease wear of PTFE, maintain low friction, and
 502 help improve adhesion of the transfer film [9]. The presence of tiny fragments of glass fibers in the
 503 transfer film that is mostly comprised of PTFE may hence help explain the stability of friction and
 504 low wear observed.

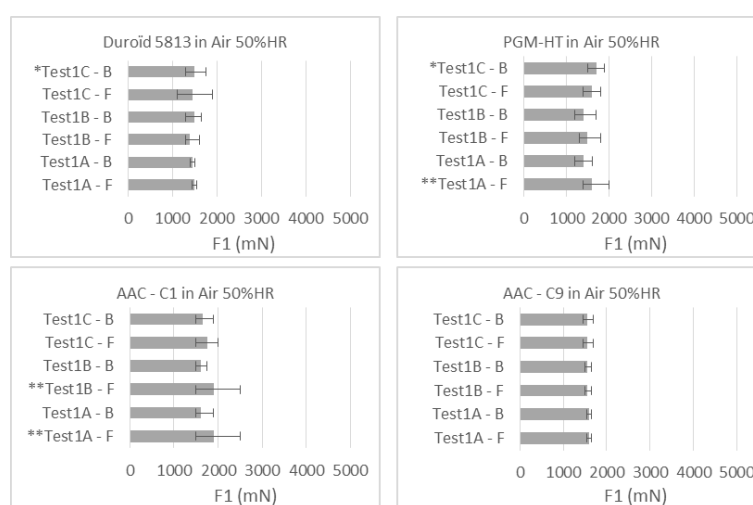
505 It is important to note that 3rd body morphologies, such as those encountered on the pad, the
 506 roller, and the plate, have been observed on bearings lubricated only by a PGM-HT cages and that
 507 have been operated in "real" conditions on a bearing test set up [36].

508 Finally, EDS analyses show that in some cases, traces of Fe iron can be found in the contact
 509 ellipse, especially with PGM-HT. This seems to be in agreement with other studies [1,20] which state
 510 that the size of the fibers can influence/increase the abrasion of the metal counter surface and
 511 consequently the detachment of material from the latter.

512 3.2. Tests in Air 50%RH environment

513 For each material, only one test gathering the 3 phases A, B, and C was carried out under air due
 514 to very limited number of samples. However, the stability of the friction all over the test duration
 515 makes it worth presenting them in this section. All 3D representations of F1 as a function of cycle
 516 number and track length can be found in supplementary information SI.2.

517 3.2.1. Friction force



518

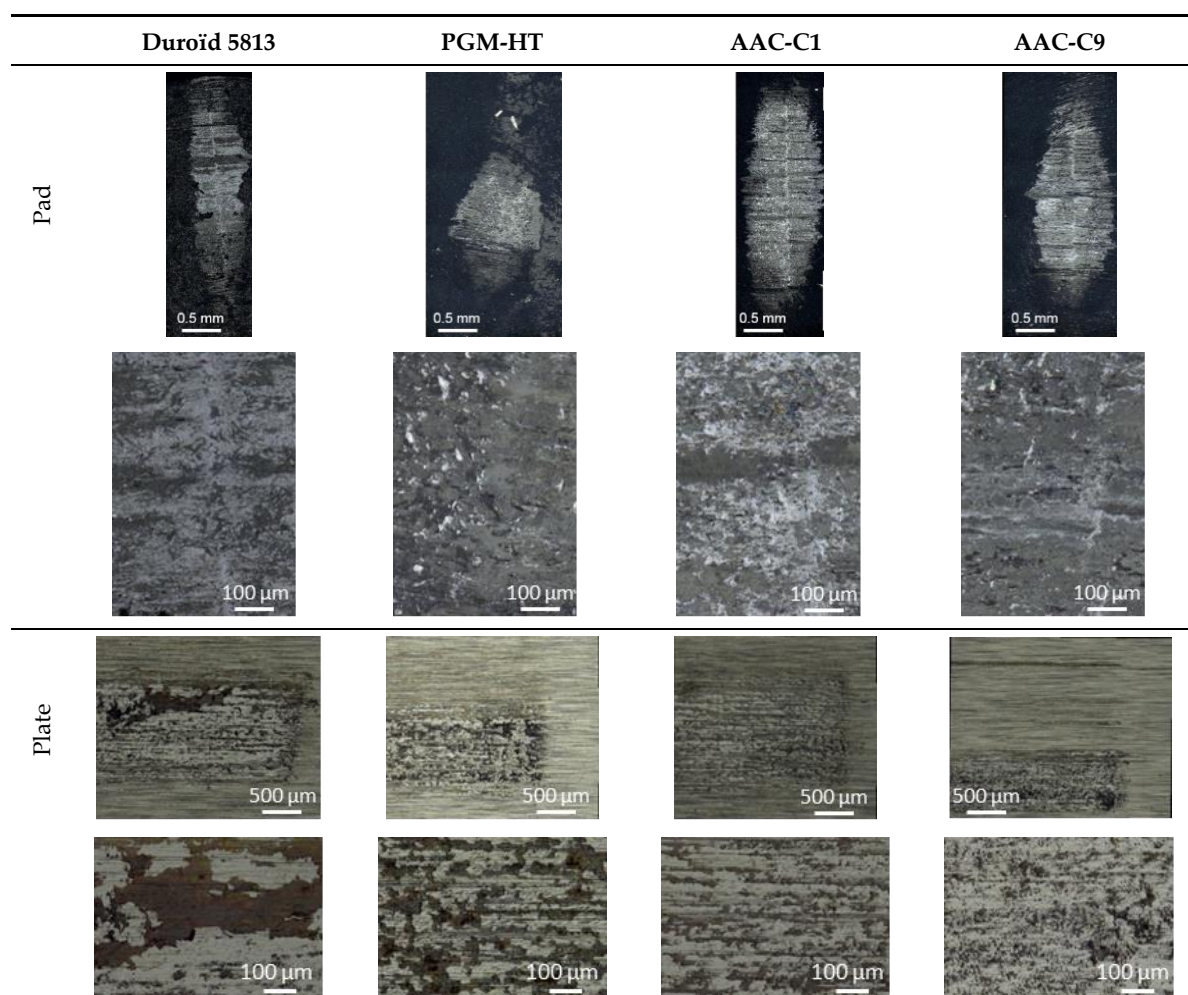
519 **Figure 6** - Variation of normal force F1 at the contact between the composite pad and the roller after
 520 test in Air 50%RH. B and F refers to Backward and Forward motion of the alternative sliding direction.
 521 Errors bars represent the min/max amplitude of F1 during the test. * refers to high min/max variations
 522 originating from noise, and ** originating from big particles circulation inside the contact.

523 Contrary to the tests under UHV, the variations in F1 in air 50%RH (**Figure 6**) exhibit an
 524 extremely low amplitude of variation and the absence of noise, for all composites. PGM-HT is much
 525 more stable than in UHV environment. Nonetheless, it shows big particle circulation inside the
 526 contact in phase A, and little noise in phase C. Duroïd 5813 is also very stable and exhibit little noise
 527 in phase C similarly to PGM-HT. AAC-C9 composite exhibits the most stable behavior out of the
 528 three composites. It shows very high stability and better tribological behavior (F1 force wise) than the
 529 Duroïd 5813, PGM-HT, and AAC-C1 composites. AAC-C1 composite exhibits variations that are
 530 similar to those observed for Duroïd 5813 and PGM-HT composites. Its behavior nonetheless stays
 531 close to what is observed in UHV in **Figure 2**.

532 3.2.2. Surface analysis

533 The test consisted of 3 phases A, B and C. It is difficult to make a clear statement on the evolution
 534 of the transfer during each phase, although regular eye inspection of the samples was done through
 535 a side glass window while the tests were running. The qualitative evaluation of the transfer presented
 536 in the section is therefore done over the 3 phases.

537 **Table 7** - Optical images of the contact area on the composite pad and the plate samples



538 Duroïd 5813 presents the "coarsest" transferred layer. It is made up of "patches/clusters" of
 539 material whose size is significantly larger than what is observed under UHV. Patches' distribution
 540 nevertheless appears relatively homogeneous. PGM-HT demonstrate similar morphologies with
 541 some big patches. For both PGM-HT and Duroïd 5813, the volume of particles ejected from the
 542 contact on the pad seems less important than that observed under UHV. However, the ejected
 543 material appears rather compact.
 544

545 AAC-C1 presents a transferred layer with a granular aspect, less "smooth" than what it observed
546 after the tests under UHV. The distribution and size of the patches appears similar to what was
547 observed after test in UHV. It is formed of "patches/clusters" of material whose size is smaller than
548 that observed under air 50%RH with PGM-HT and Duroïd 5813. It is interesting to note that although
549 it demonstrates the creation of large particle on F1 variations (**Figure 6**), no large patches are observed
550 on the wear tracks as compared to the 3 other composites (**Table 7**). On the pad, the volume of
551 particles ejected seems close to that observed under UHV and seems to be between that observed
552 under air 50%RH for Duroïd 5813 and PGM-HT.

553 AAC-C9 is very similar to AAC-C1. Indeed, it presents a transferred layer with a granular aspect,
554 less "smoothed" than that observed after the tests under UHV. It is formed of both large
555 "patches/clusters" of material whose size is smaller than that observed under air with PGM-HT and
556 Duroïd 5813, and of small cluster evenly distributed across the friction track. The small cluster are
557 much smaller than those created by AAC-C1, but the big ones are bigger than the biggest observed
558 with AAC-C1. The contact ellipse is fairly homogeneous with a few particles ejected in the vicinity of
559 the contact. However, the volume of particles ejected seems less important than that observed under
560 UHV and seems to be close to that observed under air for Duroïd 5813. AAC-C9 is exhibiting the
561 lowest volume of particles.

562 Overall, **Table 7** shows that the transferred material observed on the plate is coarser than what
563 is observed after test in UHV, for all composite materials. The distribution of material seems
564 nevertheless relatively homogeneous. The contact ellipse on the pad is fairly homogeneous with a
565 few particles ejected in the vicinity of the contact. A smaller ejection distance of the particle away
566 from the contact is not unique to the composites. It can be observed for MoS₂ lubricated bearing tests
567 between UHV and N₂ [55]. Interestingly, PGM-HT, Duroïd 5813, and AAC-C9 exhibit lower volume
568 of ejected particles as compared to UHV test. AAC-C9 is the composite exhibiting the lowest volume
569 of particles. AAC-C1 does not exhibit significant changes in term of particle creation and ejection as
570 compared to UHV tests. Krick [56] observed smaller debris created from PTFE material sliding in
571 humid environment as compared to dry environment. AAC-C1 demonstrated the capability to
572 adsorb residual water from the vacuum chamber. That may explain the absence of significant changes
573 for AAC-C1, and the changes observed for the 3 other composites when tested in UHV and in humid
574 air. The presence of water consequently appears favorable to PGM-HT, Duroïd, and AAC-C9, and
575 most likely helps in anchoring the PTFE based transfer film [16]. However, Dark field light
576 microscopy images show some coloration of the 3rd body with brown-orange and yellowish colors,
577 particularly visible with Duroïd 5813 and PGM-HT. This color could indicate molybdenum oxide
578 formation. Humidity and molybdenum oxides are known to impede MoS₂ to reduce friction and
579 wear [53,57]. Better anchorage of PTFE may help mitigate the negative impact of MoS₂ oxidation.

580 Therefore, the differences observed in F1 variations between tests conducted in UHV and in Air
581 for PGM-HT, Duroïd 5813 and AAC-C9 in general are most likely due to delamination [12] and big
582 particles circulation inside the contact, and the lack of water that prevent sufficient adhesion of the
583 transfer film to the substrate [16,56]. Nonetheless, the oxidation possibly related to MoS₂ observed in
584 air, particularly visible with Duroïd 5813 and PGM-HT, both of which exhibit noise in phase C, may
585 impede the improved transfer when significant shear stress is applied to the transfer film. Noise could
586 also be related to stick-slip and/or material stiffness that may not damp the vibrations emanating
587 from the contact.

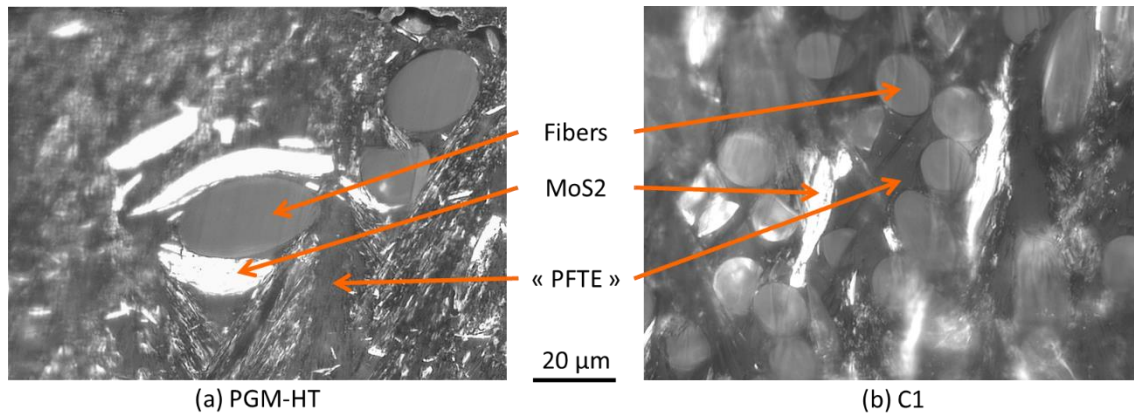
588 Considering the quality and distribution of the transfer layer and the stability of F1, AAC-C9
589 appears to be a good candidate, as well as AAC-C1.

590 3.3. Adhesion measurement

591 Adhesion measurement have first been carried out on both bulk and friction track (from double
592 transfer experiments) of PGM-HT and AAC-C1 composites and thus under laboratory conditions
593 (laboratory humid air and room temperature). For the most promising composite AAC-C1, a
594 dedicated study has been conducted to evaluate the influence of both environment and temperature
595 on adhesion.

596

3.3.1 Adhesion between **bulk composite** material and AISI440C bead under laboratory conditions



597

598

599

Figure 7 - Optical observation of local composition and morphology of bulk of (a) PGM-HT and (b) AAC-C1 after ion milling

600

601

602

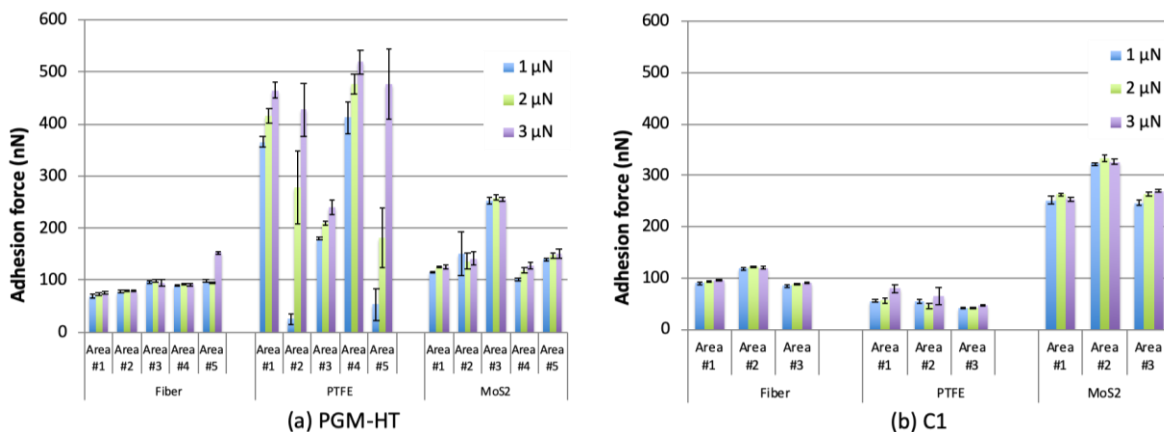
603

604

605

606

Elementary components of both composites are easily distinguishable on **Figure 7**. Bright areas are MoS₂ particles, light grey elliptical areas are fibers, and mixed bright/dark areas are the “PTFE” matrix which surround MoS₂ and fibers. Those optical observations, coupled with SEM using Z-contrast mode when necessary, were used to help positioning the cantilever of the AFM, and interpreting AFM images. Such approach allowed to clearly associate adhesion measurement with the material of interest, i.e. MoS₂, PTFE, and fiber.



607

608

609

Figure 8 - Local measurement of adhesion force after different loading values for each component of (a) PGM-HT and (b) AAC-C1

610

611

612

613

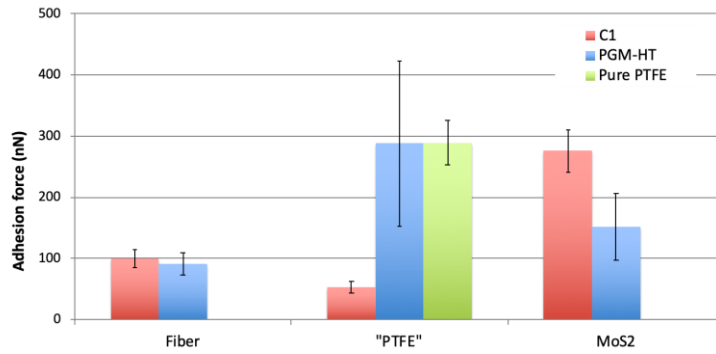
614

615

616

617

Adhesion forces measured on the different locations and for each normal load are gathered in **Figure 8**. Overall, the adhesion force measured is not significantly sensitive to the applied load except, for the PTFE of the PGM-HT whatever the area considered. If the reason for such an observation was the softness of PTFE (it is the softest material out of the 3 components of the composite) similar behavior would have been observed with AAC-C1, unless the PTFE stiffness is significantly different between both composites. Stress concentration at the contact between the bead and the PTFE may induce mechanically activated reaction with water and create bonding between the bead and the PTFE. Further investigation is needed to fully understand such behavior.



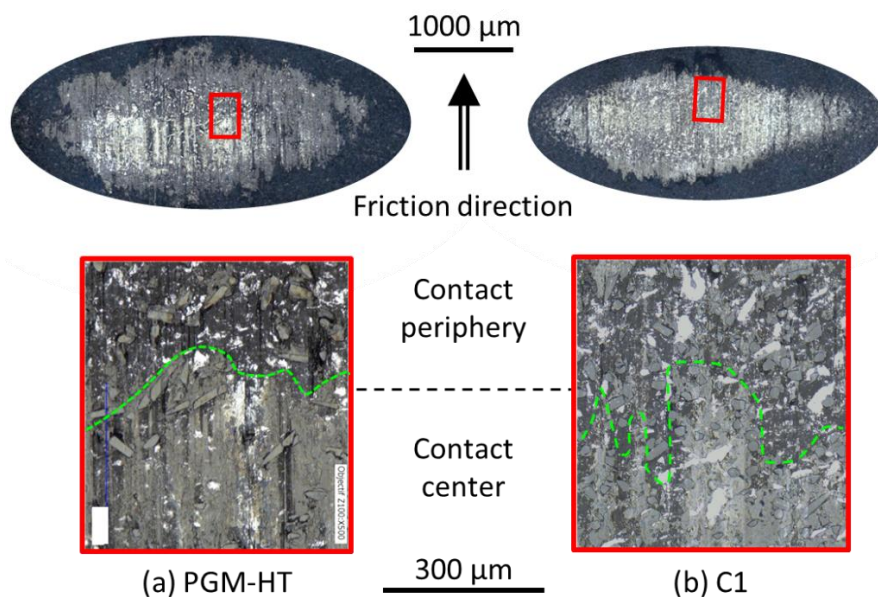
618
619
620

Figure 9 – Mean adhesion force and associated standard deviation (black lines) for each component of pure PTFE, PGM-HT and AAC-C1

621 To compare the general trends of adhesion respectively to each component for both composites,
622 the mean value and the standard deviation of the pull of force measured on each and every
623 component are computed and displayed on **Figure 9**. Fibers from both composites exhibit similar
624 adhesion to AISI440C steel with an adhesion force evaluated around 100 nN. Furthermore, the
625 standard deviation shows that dispersion in the measurement is very low across both composites
626 (**Figure 8** and **Figure 9**). For MoS₂ and PTFE, opposite trend is observed. Even considering the large
627 dispersion in the measure (high standard deviation), the adhesion force obtained on the PTFE from
628 the PGM-HT remains between 3 to 8 times higher than for the one obtained with AAC-C1. Note that
629 the mean value of PTFE adhesion from the PGM-HT is close to the one measured on a sample of pure
630 PTFE from the reference sample. Within a smaller range, the opposite is highlighted for MoS₂ where
631 the mean adhesion force is nearly twice as higher for AAC- C1 than for PGM-HT.

632 Consequently, the adhesion between the components of the composites and the AISI440C steel
633 is in favor of a greater transfer of MoS₂ to the contacting surface for composite AAC-C1, which may
634 participate to the creation of a more tribologically efficient 3rd body layer. The proportion of MoS₂
635 within the 3rd body (presence evidenced in **Figure 5**, spectrum S_i) could indeed be higher and help
636 lubrication in UHV. To the contrary, in air, it may impede the friction, which would partly explain
637 the highest variability of F₁ in air as compared to UHV (**Figure 2** and **Figure 6**).

638 3.3.2 Adhesion between *friction tracks of composite material and AISI440C bead under laboratory*
639 *conditions*



640
641
642

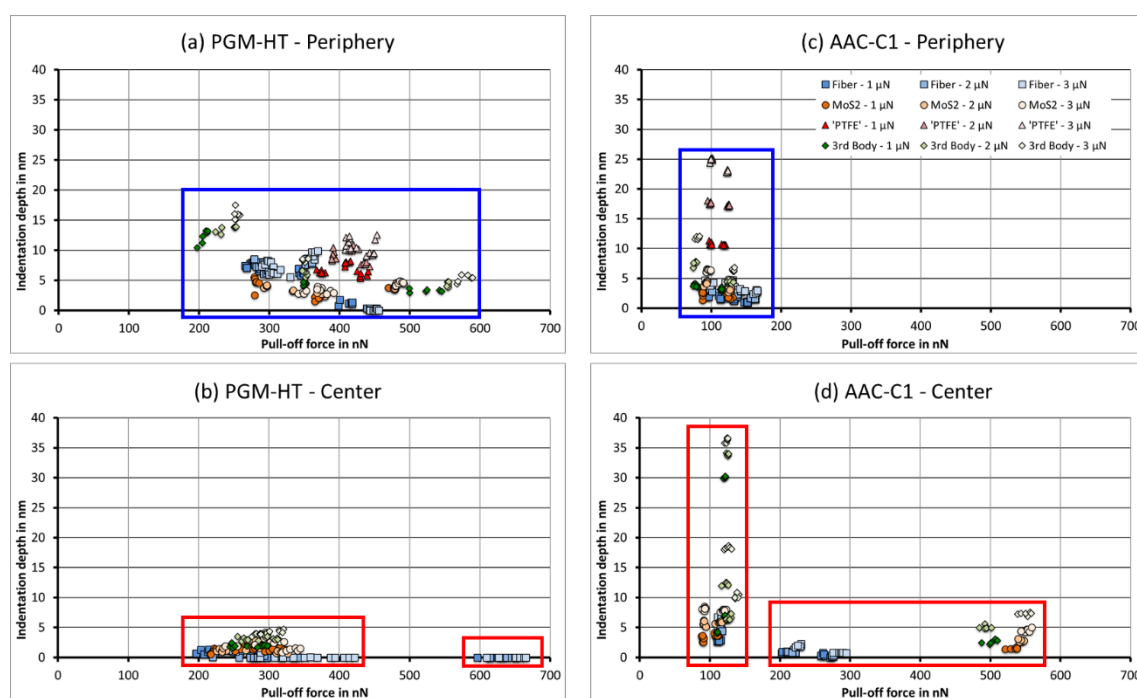
Figure 10 – Optical observation of local composition and morphology of friction tracks of (a) PGM-HT and (b) C1

643 Adhesion measurements have also been done on AAC-C1 and PGM-HT composites after
 644 complete (phases A, B, and C) double transfer tests (see § 2.1.1). Optical microscope images of the
 645 friction tracks of both composites are shown on **Figure 10**. Two distinct regions are defined: the
 646 contact periphery and the contact center. The latter corresponds to the contact ellipse. Their main
 647 difference to differentiate both regions lies in the higher presence of 3rd body particles at the periphery
 648 of the contact than at its center.

649 Multiple locations have been selected in both region on each composite. However, bar graph
 650 representations could not help dissociating components. It has been chosen to plot the adhesion force
 651 as a function of the indentation depth (**Figure 11**). Such representation gives access to a qualitative
 652 comparison of the stiffness of the materials where the adhesion force is measured. The higher the
 653 value of indentation depth is, the lower is the stiffness of the tested material. As MoS₂ and fiber are
 654 stiffer than the PTFE, it can be expected that indentation depth helps dissociating materials and that
 655 clusters of adhesion forces will be identified. Note that the 3rd body is a mix of several materials and
 656 so its stiffness will be very variable; its composition cannot be reliably determined through the
 657 indentation depth measurement.

658 Finally, the surfaces studied are real friction surfaces. A thin layer of 3rd body transparent to light
 659 may exist on top of each material even if it looks like pristine one (especially for fibers or MoS₂
 660 particles). A difference may consequently appear on both indentation depth and adhesion force
 661 measured in comparison to the one measured on IM prepared bulk material. To preserve the contact
 662 characteristics, the choice has been made not to ion mill or clean the friction surface.

663 **Figure 11** shows two distinct distribution between the periphery and the center regions of the
 664 contact for both composites. Note that in the center of the contact, no PTFE data is presented. The size
 665 of the bead and the surface geometry made it impossible to be certain the PTFE region were
 666 confidently characterized.
 667



668 **Figure 11** – Comparison of the adhesion forces between the center of the friction track and its
 669 periphery for PGM-HT (a – periphery / b – center) and C1 (c – periphery / d – center)
 670

671 For PGM-HT, the periphery of the contact is characterized by values of adhesion forces mostly
 672 in the range of 250 nN to 450 nN, which corresponds to the range of PTFE related adhesion forces
 673 in the bulk (**Figure 9**). Interestingly, the PTFE at the periphery exhibits pull-forces in the higher range
 674 of the forces measured on the bulk. Compared to the center region, the fiber and MoS₂ materials
 675 appear soft, the indentation depth goes up to 10 nm and 6 nm respectively while it is in the range of

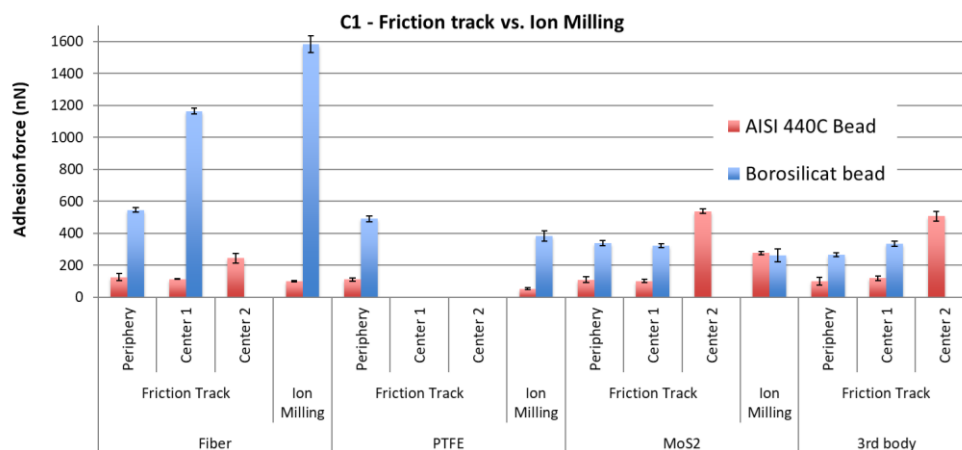
0 nm to 3 nm in the center. That is in line with PTFE coverage. The 3rd body demonstrates highly dispersed values of adhesion force with 3 clusters in the ranges of 200 nN to 250 nN, 350 nN, and 500 nN to 600 nN irrespective of the normal force applied for the measures. In the center, the fibers demonstrate two clusters of adhesion force values, one in the range 200 nN to 420 nN and one in the range 600 nN to 670 nN. All other materials are undistinguishable and are clustered in the 200 nN to 350 nN range, which is in the range of PTFE related adhesion forces in the bulk (**Figure 9**), but in a much narrower distribution as compared to the periphery. Indentation depth is also very low and below 5 nm. It seems that in the center of the contact the material is very stiff. A first set of data shows that MoS₂, fibers, and 3rd body exhibit similar adhesion than PTFE from the bulk, which suggest the center of the contact is covered with thin PTFE based material. It also has exposed fibers that exhibit very high adhesion with AISI440C (600 to 700 nN). The stiff contact may be prone to enhanced propagation of instabilities with low transfer (thin PTFE layer) as depicted in previous sections. Moreover, if the relatively high stiffness of the PTFE (as suggested by the indentation depth) may contribute to excessive damage in the composite, particularly at the fiber/PTFE interface and promote the creation of large fiber based debris [58]. The stickiness of the fiber may further contribute to a higher risk of excessive wear of the steel counterpart or of the composite itself as it may increase the risk of delamination. This particularly true when it is colinear to the sliding direction [12]. If the fiber is orthogonal to the contact, then it might benefit from the adhesion and be further eroded to create small particles that would enhance the transfer film properties [9,10,59]. In the case of PGM-HT, a large number of fibers are aligned colinear to the sliding direction. The matrix stiffness, the stickiness of fiber to steel, and the fibers alignment, altogether explain the torque noise during bearing test and steel particle presence inside and around the bearing [1], and the detection of Fe inside the contact ellipse on the pad (cf. section 3.1.3).

For C1, the periphery of the contact is characterized by a narrower range of adhesion forces centered on lower values than for the PGM-HT. The range extends from 80 nN to 180 nN. Such range is in good agreement with the values of adhesion forces measured on PTFE and fibers on the bulk material (**Figure 8**). MoS₂ corresponding values are 3 times lower as compared to the bulk material, meaning potential coverage by PTFE. Indentation depth are in good agreement with the materials: PTFE exhibits high indentation depths that are increasing with increasing normal loads, fibers and MoS₂ are exhibiting indentation depth in the range of 2 to 5 nm which is in line with a much stiffer material. The 3rd body material lies between MoS₂/fiber and PTFE clusters in term of indentation depth which makes sense considering it is a mixture of all 3 components. The adhesion force value makes it however closer to PTFE which may indicate a high proportion of PTFE in it. This is in line with the matrix stiffness compared to PGM-HT, and with the large proportion of fibers orthogonal to the contact, both inducing lower risk of delamination and large fiber fragment detachment [12,58]. The center of the contact is very different and adhesion values can be divided into two groups. The first one is located around 100 nN adhesion force value. In that group fiber, MoS₂, and 3rd body are found to exhibit very close adhesion values. MoS₂ and fiber are clustered with adhesion force values mostly around 90 nN for MoS₂ and 110 nN for fiber. The indentation depth associated to both of them is in the range from 3 to 9 nm which is wider than in the periphery. The indentation depth is also increasing with increasing normal load. The 3rd body is mostly distributed along 110 nN adhesion force value but in the range of 5 to 40 nm indentation depth irrespective of the normal load. In the first group the material appears soft and exhibits adhesion forces in the range representative of the fibers in the bulk material, which suggests the presence of a PTFE/fiber-based material in the locations where the measurements were made.

The second group is orthogonal to the first one with mostly low indentation depth (below 8 nN) but a wide range of adhesion forces from 200 nN to 580 nN. This group gathers fiber, MoS₂ and 3rd body. However, it can be subdivided into two other subgroups. The first subgroup is solely comprised of fiber related data. Fibers are very stiff (indentation depth below 3 nm) but quite adhesive (200 nN to 300 nN adhesion force). Interestingly, in this subgroup, adhesion forces are mostly within the range representative of MoS₂ with regards to the bulk material (**Figure 9**). The second subgroup is comprised of MoS₂, and 3rd body related data, it is located in the high range of

728 adhesion forces (450 nN to 550 nN). They dissociate very well the materials. MoS₂ related data in the
 729 510 to 550 nN range with indentation depth running from 2 nm to 5 nm, both adhesion forces and
 730 indentation depth increase with increasing normal load. 3rd body related data is in the 480 to 550 nN
 731 adhesion force range and in the 3 to 8 nm indentation depth range. The latter is increasing with the
 732 normal load, while the former jumps from 480 nN to 550 nN when the normal load increases from 2
 733 μN to 3 μN. MoS₂ and 3rd body related materials are stiff and might be covered with PTFE based
 734 material (indentation depth increasing with increasing normal load), however it must be very thin. It
 735 might also be a different compaction level as compared to the less adhesive first group, such as the
 736 observed materials on the plate (**Figure 5** and **Table 6**). The high values of adhesion forces can be
 737 related to a possible activation of the surface by friction. In the second group fibers are more adhesive
 738 than on the bulk, which is similar to what was observed with PGM-HT. It is, however, interesting to
 739 note that the most adhesive materials are the 3rd body and the MoS₂, and that the least adhesive is the
 740 fiber whose adhesion forces is in the range of MoS₂ values measured on the bulk. That might mean
 741 that the activation of surfaces by friction induce high adhesion of MoS₂, which transfers easily to get
 742 mixed with PTFE and fibers, and takes over the adhesion behavior. That would consequently reduce
 743 further the risk of detachment of fiber. Which would be in line with assumption made from F1
 744 variations and surfaces analysis. In parallel, such high adhesion and transfers helps create softer and
 745 less adhesive group of materials (1st group) that most likely contain PTFE considering the high
 746 indentation depth. Numbers of data points between the two groups is almost equal for all material.
 747 The lubrication might thus be equally supported by both groups with enhanced contribution of MoS₂
 748 in the creation of the 3rd body and therefore the lubrication. PTFE may help in the 3rd body creation
 749 to soften it and help in the damping. The small fragment of fiber (the composite hard filler) may help
 750 modulating this behavior by modulating the mechanical properties of the transfer film [10,59]. Finally,
 751 the observed reactivity of AAC-C1 towards water, may help the 3rd body to adhere to still and to
 752 stabilize friction and wear [16].

753 3.3.3 Adhesion of borosilicate beads with composites materials before and after friction

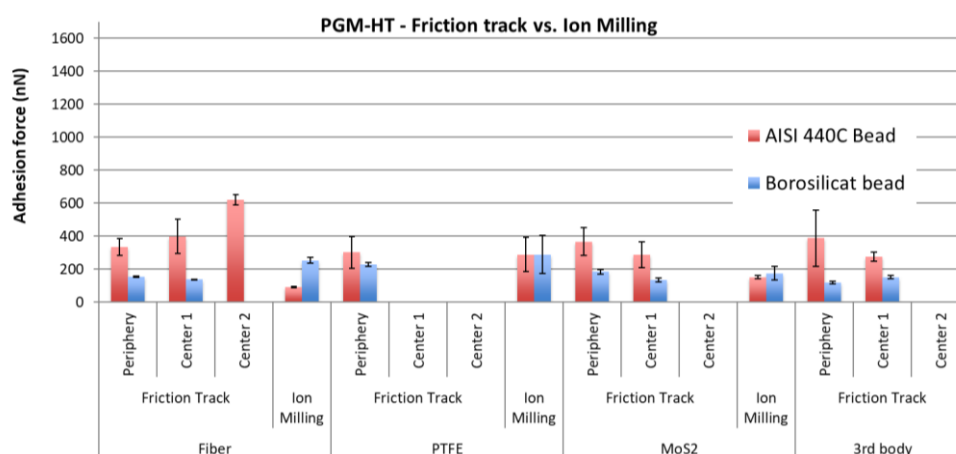


754

755 Figure 12 - Comparison of adhesion between AISI 440C steel and Borosilicate on the contact materials,
 756 for AAC-C1 composite bulk after ion milling, and after friction

757 Fibers are suggested to play an important role in the stability of friction and in the mechanical
 758 properties of the 3rd body layer. To get better insight into how significant is the fiber's contribution in
 759 the building up of 3rd body layer, adhesion measurement has been conducted using a borosilicate
 760 bead. Fiber's composition appears very close to borosilicate. **Figure 12** and **Figure 13** show the
 761 comparisons between the adhesion forces measured with both borosilicate and AISI 440C steel beads
 762 on both the composites AAC1 and PGM-HT. Measures are performed on bulk material after ion
 763 milling, and after friction. Note that there are not 2 groups in the center of the contact contrary to
 764 what was observed with AISI440C steel. Center 1 and Center 2 correspond to the groups identified
 765 in the center of the contact and displayed on **Figure 11**.

766



767

768

769

Figure 13 - Comparison of adhesion between AISI 440C steel and Borosilicate on the contact materials, for AAC-C1 composite bulk after ion milling, and after friction

770

771

772

773

774

775

776

777

778

779

780

781

782

As expected, borosilicate bead is very adhesive to the fiber for C1 and it is exhibiting very high adhesion as compared to AISI 440C steel. Overall, the borosilicate is more adhesive to the PTFE, MoS₂, and to the 3rd body, as compared to the AISI 440C steel. Adhesion to AISI 440C steel is higher than the adhesion to borosilicate for the MoS₂ and 3rd body that are located in the center of the friction track. Although significantly lower than the adhesion to the borosilicate, the adhesion of fiber to AISI 440C steel is higher in Center 2 than in Center 1. Consequently, the fiber may (1) easily and quickly retain PTFE and MoS₂ particles on its surface which can form a protective lubricious layer to slide against the steel counterparts; and (2) be a binder to build a 3rd body layer with MoS₂ and PTFE. Fibers will, however, not impede the transfer of MoS₂ and 3rd body to the steel counterpart's surface considering adhesion magnitudes can be very high in the center of the contact, which is the region where the materials are the most stressed. Such observation is also consistent with the composition of the transferred layer that has been shown (cf. section 3.1.3) to be mostly comprised of PTFE and MoS₂ based materials.

783

784

785

786

787

788

789

790

791

792

793

794

795

796

797

798

799

800

801

802

803

804

Surprisingly, the trend is completely the opposite with PGM-HT. The borosilicate is not exhibiting high adhesion with the fiber as compared to AISI 440C steel, except after IM. Magnitude of adhesion is not varying much across the materials after friction, and across both the periphery and the center of the contact. It is believed that a chemical component, maybe the sizing of the fiber, may be spread all over the contact by friction and induce a homogenization of the adhesion behavior towards borosilicate material and AISI 440C steel materials. The higher adhesion of the fiber to AISI 440C steel as compared to borosilicate for MoS₂, and 3rd body during friction could impede the creation of a protective lubricious layer on top of the fiber. Considering that the fibers are stiff and hard as compared to PTFE and the 3rd body, the contact fiber/AISI 440C (the roller) may impede the transfer via mechanical removal of the material during friction. This added to the stiff matrix, and to the alignment of fibers colinear to the sliding direction, would in turn explain (i) the lower capability of PGM-HT to transfer material to the sliding counterparts as compared to AAC-C1, and (ii) its higher propensity to generate large debris [12,58]. That overcome the fact that the 3rd body created appears more adhesive to steel than the 3rd body created from AAC-C1. There is a competition between the fibers and the other tribological materials towards steel that appears to be in favor of the fiber, leading to lower performances. It would also confirm why PGM-HT is more subjected to instabilities, and maybe Duroïd 5813 too. Noise is indeed detected for PGM-HT (Test 3A-B) and Duroïd 5813 (Test1A-B, Test1B-B, Test3A-B) in UHV (Figure 2), and during tests Test1C-B for both PGM-HT and Duroïd 5813 in air (Figure 6). Adhesion might be exacerbated in UHV due to the absence of water molecules that might accumulate on the surfaces and react with PTFE to anchor it to the steel and form the lubricious transfer film [16]. That would also explain why instabilities are not significant in humid air. Further detailed analysis would be necessary to fully understand the mechanisms involved.

805 Fibers have been shown to play a role of mechanical trap to retain 3rd body particles within the
806 contact (cf. section 3.1.3). This section now demonstrate that it can play a role of “adhesion driven
807 trap” to retain lubricious materials via their adhesion on the fiber’s surface. Good tribological
808 performances are able only an equilibrium is found between both actions.

809 4. Summary and conclusion

810 Four different self-lubricating materials have been studied and their capability to lubricate ball
811 bearing for space applications have been investigated. Among the 4 composites, 1 was commercially
812 available and fabricated until the mid-1990s (Duroïd 5813), 1 is commercially available and
813 recommended for such application (PGM-HT), and the remaining 2 are prototype composites (AAC-
814 C1 and AAC-C9) to be investigated as potential alternative to PGM-HT. PGM-HT indeed
815 demonstrated some limitations and new composites offering more stable performances are required.
816 All composites are made of PTFE, MoS₂ particles, and glass (Duroïd 5813, PGM-HT, AAC-C1) or
817 mineral (AAC-C9) fibers. A dedicated tribometer that allows to simulate the double transfer
818 lubrication has been designed for the study. The decision made to give degrees of freedom to the
819 composite pad to allow it to move around its central position has been decisive in reproducing
820 transfer in terms of particle and layers morphologies. Such freedom is believed to reproduce the ball
821 bearing cage’s freedom when it is in contact with the ball during ball bearing use.

822 Test in UHV and in air environment allowed to demonstrate that AAC-C1 could be a good
823 candidate to replace both Duroïd 5813 and PGM-HT. The tribological behavior is indeed very good
824 (good transfer capability and stable friction). The tribological tests coupled with mass spectrometry
825 measurements, and AFM based adhesion measurements on the bulk materials on the worn and
826 unworn materials showed that the reasons for AAC-C1 to perform the best as compared to PGM-HT
827 are:

- 828
- 829 • Mass spectrometry measurement showed that one important element is the continuous
830 transfer of material all along the test, without damaging nor wearing too much the
831 composite. It can be compared to smooth erosion rather than abrasion.
- 832 • Low delamination issue due to fiber orientation mostly orthogonal to the contact. That lead
833 to stronger capabilities of smooth erosion of fiber, which in turn lead to nanoparticle creation
834 that were mixing to the transferred material. That helped to provide relevant mechanical
835 properties to the transfer film to accommodate velocities, even during severe rolling plus
836 sliding configuration.
- 837 • Lower matrix stiffness which reduces the risk of volume damage and the creation of large
838 debris (mostly from fibers), and the possible occurrences of instabilities
- 839 • Adsorption of residual water inside the vacuum chamber in phase A, gentle running which
840 is believed to lead to better transfer and anchorage of the transferred material. That can
841 constitute a big advantage during the first months, even the first year of service in orbit for
842 satellite. Due to surface and material outgassing, the vacuum level is low and the
843 atmosphere comprised of high level of water [60–62]. Such water can help in producing the
844 proper transfer film.
- 845 • High adhesion of MoS₂ towards steel and high adhesion of fiber towards PTFE which are
846 both in favor of the formation of lubricious transfer film. Fibers play an important role in
847 trapping the particles inside the contact on the pad surface, to ultimately create a lubricious
848 material. PGM-HT exhibits primarily high adhesion of fiber towards steel which further
849 increase the risk of the abrasion of both steel and the transferred material.
- 850 • Equilibrium between internal cohesion of transferred material, and adhesion to counterparts
851 must be satisfied

852

853 To further highlight the underlying physical, chemical, and mechanical mechanisms driving the
854 tribological behaviors of the composites, complementary investigations are needed. The effect of
855 mineral fibers (AAC-C9 case) as compared to glass fibers could be of particular interest. The

856 complementary investigations include further adhesion/cohesion investigation in different
 857 environments, the effect of the sizing of the fiber, and numerical modelling of the contacts to get
 858 insight of the tribological behavior by entering virtually inside the contact.

859 **Supplementary Materials:** The following are available online at www.mdpi.com/xxx/s1, Figure S1: drawing of
 860 the roller specimen, Figure S2: Friction forces F_1 during test in UHV, Figure S3: Friction force F_1 during tests in
 861 Air 50%RH, Figure S4: Picture and optical microscope images of the roller after Phase A test in UHV, Figure S5:
 862 Mass Spectra of PGM-HT, AAC-C9 composites, and AAC-C1 with water variation, S6: Probable error sources of
 863 the experimental data.

864 **Author Contributions:** test on the DTTB, analysis of the results and post-test characterization of the samples, G.
 865 Colas under the supervision of A. Saulot and Y. Michel; discussion of the tribological test results, G. Colas, A.
 866 Saulot, A. Merstallinger, Y. Michel; adhesion test conceptualized by G. Colas, A. Saulot, and T. Filleter,
 867 performed by A. Saulot, and G. Colas, analyzed by A. Saulot, G. Colas, and T. Filleter; composite designed and
 868 provided by A. Merstallinger. Overall discussion of the results and preparation of the paper by all co-authors.
 869 All authors have read and agreed to the published version of the manuscript.

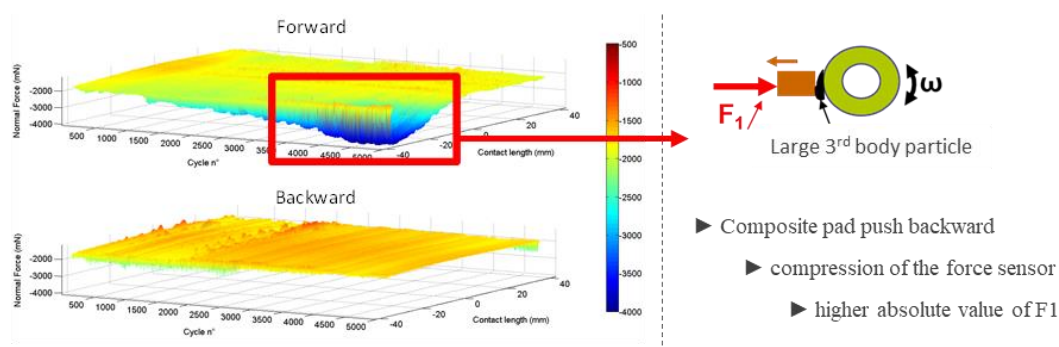
870 **Funding:** This research was funded by multiple funding from the French Space Agency CNES (R&T R-S10/TG-
 871 0002-009 and DCT/TV/MS – NT.2010- 10096), from the European Space Agency (“EU Self Lubricating materials
 872 SLPMC2”, Contract No. 4000115464/15/UK/ND), and from Canada (CFI and NSERC).

873 **Acknowledgments:** the authors are very grateful to Simo Pajovic (summer student at the University of Toronto)
 874 who helped in the gluing of AISI 440C beads on the cantilevers, to Matthew Daly (PhD student at the time in the
 875 Material Science and Engineering department of the University of Toronto) and Sal Boccia (Engineer at the
 876 OCCAM, University of Toronto) for their help in the ion milling of the composite samples), to Claude Godeau
 877 (Engineer at LaMCoS, Lyon) who helped conducting the experiments on Pedeba tribometer, to Yves Berthier
 878 (CNRS Research Director, LaMCoS, Lyon) for is contribution in the discussion of the results.

879 **Conflicts of Interest:** The authors declare no conflict of interest.

880

881 Appendix A



882

883 Figure A 1 - Schematic of the effect of particle circulation on the F_1 measure

884 The significant events such as big particle detachment or circulation inside the contact (cf. **Figure**
 885 **2** and Figure A 1) increases in motor torque noise (related to current consumption), are strongly
 886 amplified in the normal load F_1 . Consequently, F_1 efficiently helps to discriminate the materials and
 887 link their behavior to both the composite and the 3rd body constitutions, morphology, etc. The motor's
 888 current consumption is indeed approximately the same for each material, as well as the tangential
 889 force measured at the contact between the roller and the plate. For the latter, the measured force is
 890 extremely low (close to the lower limit of measuring range) due to the rolling motion. A significant
 891 increase implies high adhesion, if not cold-welding, at the contact, i.e. failure of lubrication.

892

893

894

895

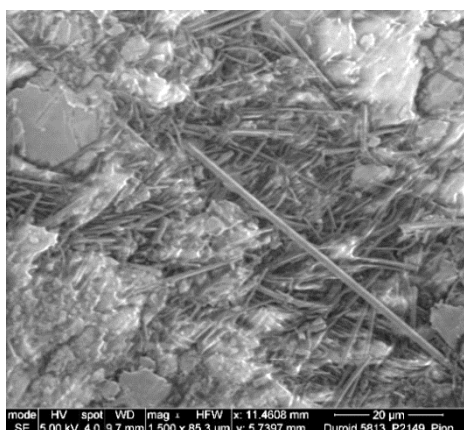
896 **Appendix B**

Figure A 2 - SEM image of the bulk of the Duroïd 5813 composite material. It shows the fibers gathered as bundles and clusters within the Duroïd 5318

907 **References**

- 908 [1] J. Sicre, Y. Michel, E. Videira, L. Nicollet, D. Baud, PGM-HT as RT/Duroïd 5813 replacement? Lifetime
 909 results on STD earth scanning sensor and polder bearing shaft, Proc. 13th Eur. Sp. Mech. Tribol. Symp.
 910 - ESMATS 2009 (ESA SP-670). ESA SP 670 (2009).
- 911 [2] E.W. Roberts, Space Tribology Handbook 5th Edition, European Space Tribology Laboratory,
 912 Warrington, U.K, 2013.
- 913 [3] J.R. Lince, Effective Application of Solid Lubricants in Space Mechanisms, Lubricants. 8 (2020) 74.
 914 <https://doi.org/https://doi.org/10.3390/lubricants8070074>.
- 915 [4] M. Buttery, B. Wardzinski, K. Houton, W. House, B. Park, Modern self-lubricating composites for space
 916 applications: PGM-HT and Sintimid 15M, in: ESA (Ed.), Proc. 14th Eur. Sp. Mech. Tribol. Symp. -
 917 ESMATS 2011, Constance, Germany, 2011: pp. 87–94.
- 918 [5] G. Theiler, T. Gradt, Friction and wear of PEEK composites in vacuum environment, Wear. 269 (2010)
 919 278–284. <https://doi.org/10.1016/j.wear.2010.04.007>.
- 920 [6] B.A. Krick, A.A. Pitenis, K.L. Harris, C.P. Junk, W.G. Sawyer, S.C. Brown, H.D. Rosenfeld, D.J. Kasprzak,
 921 R.S. Johnson, C.D. Chan, G.S. Blackman, Ultralow wear fluoropolymer composites: Nanoscale
 922 functionality from microscale fillers, Tribol. Int. 95 (2016) 245–255.
 923 <https://doi.org/10.1016/j.triboint.2015.10.002>.
- 924 [7] H.S. Khare, A.C. Moore, D.R. Haidar, L. Gong, J. Ye, J.F. Rabolt, D.L. Burriss, Interrelated Effects of
 925 Temperature and Environment on Wear and Tribochemistry of an Ultralow Wear PTFE Composite, J.
 926 Phys. Chem. C. 119 (2015) 16518–16527. <https://doi.org/10.1021/acs.jpcc.5b00947>.
- 927 [8] P. Johansson, P. Marklund, M. Björling, Y. Shi, Effect of humidity and counterface material on the friction
 928 and wear of carbon fiber reinforced PTFE composites, Tribol. Int. 157 (2021) 106869.
 929 <https://doi.org/10.1016/j.triboint.2021.106869>.
- 930 [9] S. Bahadur, D. Tabor, The wear of filled polytetrafluoroethylene, Wear. 98 (1984) 1–13.
 931 [https://doi.org/10.1016/0043-1648\(84\)90213-8](https://doi.org/10.1016/0043-1648(84)90213-8).

- 932 [10] G. Deli, X. Qunji, W. Hongli, Physical models of adhesive wear of polytetrafluoroethylene and its
933 composites, *Wear*. 147 (1991) 9–24. [https://doi.org/10.1016/0043-1648\(91\)90115-B](https://doi.org/10.1016/0043-1648(91)90115-B).
- 934 [11] J. Khedkar, I. Negulescu, E.I. Meletis, Sliding wear behavior of PTFE composites, *Wear*. 252 (2002) 361–
935 369. [https://doi.org/10.1016/S0043-1648\(01\)00859-6](https://doi.org/10.1016/S0043-1648(01)00859-6).
- 936 [12] S. Nak-Ho, N.P. Suh, Effect of fiber orientation on friction and wear of fiber reinforced polymeric
937 composites, *Wear*. 53 (1979) 129–141. [https://doi.org/10.1016/0043-1648\(79\)90224-2](https://doi.org/10.1016/0043-1648(79)90224-2).
- 938 [13] S. Qu, K.H. Lo, S.S. Wang, Effect of Transfer Films on Friction of PTFE/PEEK Composite, *J. Tribol.* 143
939 (2021) 1–11. <https://doi.org/10.1115/1.4048273>.
- 940 [14] W. Cui, K. Raza, Z. Zhao, C. Yu, L. Tao, W. Zhao, W. Chen, S. Peng, Q. Xu, L. Ma, Y. Hu, D. Liao, B.
941 Liang, T. Wang, T. Ma, Role of transfer film formation on the tribological properties of polymeric
942 composite materials and spherical plain bearing at low temperatures, *Tribol. Int.* 152 (2020) 106569.
943 <https://doi.org/10.1016/j.triboint.2020.106569>.
- 944 [15] N.L. McCook, D.L. Burris, P.L. Dickrell, W.G. Sawyer, Cryogenic friction behavior of PTFE based solid
945 lubricant composites, *Tribol. Lett.* 20 (2005) 109–113. <https://doi.org/10.1007/s11249-005-8300-4>.
- 946 [16] K.L. Campbell, M.A. Sidebottom, C.C. Atkinson, T.F. Babuska, C.A. Kolanovic, B.J. Boulden, C.P. Junk,
947 B.A. Krick, Ultralow Wear PTFE-Based Polymer Composites - The Role of Water and Tribochemistry,
948 *Macromolecules*. 52 (2019) 5268–5277. <https://doi.org/10.1021/acs.macromol.9b00316>.
- 949 [17] G.C. Birur, G. Siebes, T.D. Swanson, Spacecraft Thermal Control, in: *Encycl. Phys. Sci. Technol.*, Elsevier,
950 2003: pp. 485–505. <https://doi.org/10.1016/b0-12-227410-5/00900-5>.
- 951 [18] C. Neugebauer, M. Falkner, R. Schermann, K. Weidlich, C. Demaret, High precision duplex bearing with
952 thermal off-load device for the nirspec wheel support mechanisms, in: *Proc. 12th Eur. Sp. Mech. Tribol.*
953 *Symp.*, 2007: pp. 19–21.
- 954 [19] E.W. Roberts, *Space Tribology Handbook*, (2007).
- 955 [20] C. Martin, J. Sailleau, P. Pesenti, Expérimentation des composites autolubrifiants pour roulements
956 spatiaux, *La Rech. Spat.* (1974) 20–24.
- 957 [21] P.L. Conley, *Space Vehicle Mechanisms: Elements of Successful Design*, John Wiley and Sons, 1998.
- 958 [22] J.R. Jones, *Lubrication, Friction, and Wear* NASA/SP-8063, 1971.
959 <https://doi.org/10.1002/9781118907948.ch6>.
- 960 [23] M.N. Gardos, Self-lubricating composites for extreme environment applications, *Tribol. Int.* 15 (1982)
961 273–283. [https://doi.org/10.1016/0301-679X\(82\)90084-6](https://doi.org/10.1016/0301-679X(82)90084-6).
- 962 [24] R.L. Fusaro, Self-lubricating polymer composites and polymer transfer film lubrication for space
963 applications, *Tribol. Int.* 23 (1990) 105–122. [https://doi.org/10.1016/0301-679X\(90\)90043-O](https://doi.org/10.1016/0301-679X(90)90043-O).

- 964 [25] M. Roussel, C. Martin, J. Sailleau, Matériaux composites autolubrifiants pour utilisations spatiales, in:
965 1st Eur. Sp. Tribol. Symp. - ESA SP-111, Frascati, 1975.
- 966 [26] M.J. Anderson, Tribometer characterisation tests and definition of bearings screening plan. ESA-ESTL-
967 TM-226 01, 1999.
- 968 [27] M. Palladino, Report on ESA recommendations regarding PGM-HT use for space applications, 2012.
- 969 [28] M. Buttery, M. Cropper, E.W. Roberts, Thermally Conditioned PGM-HT - ESA-ESTL-TM-0069, 2011.
- 970 [29] G. Colas, S. Pajovic, A. Saulot, M. Renouf, P. Cameron, Adhesion Measurements in MoS₂ Dry Lubricated
971 Contacts to Inform Predictive Tribological Numerical Models: Comparison Between Laboratory-Tested
972 Samples and Ball Bearings From The NIRISS Mechanism, in: Conf. Proc. 17th Eur. Sp. Mech. Tribol.
973 Symp., Hatfield, UK, 2017. <http://esmats.eu/esmatspapers/pastpapers/pdfs/2017/colas.pdf>.
- 974 [30] C. Macho, A. Merstallinger, G. Bodrowski-Hanemann, M. Palladino, L. Pambaguian, SLP_{MC} - Self
975 Lubricating Polymer Matrix Composites, Proc. 15th Eur. Sp. Mech. Tribol. Symp. - ESMATS 2013. ESA-
976 SP-718 (2013) 8pp.
- 977 [31] I. Kohen, D. Play, M. Godet, Effect of machine rigidity or degrees of freedom on the load-carrying
978 capacity of wear debris, *Wear*. 61 (1980) 381–384. [https://doi.org/10.1016/0043-1648\(80\)90300-2](https://doi.org/10.1016/0043-1648(80)90300-2).
- 979 [32] H. Czichos, S. Becker, J. Lexow, The Versailles Project on Advanced Materials and Standards (VAMAS
980) on wear test methods is one of the rapidly growing suite of projects initiated as a result of decisions
981 following the 1982 Versailles Summit Meeting of the Heads of State or Governments , 114 (1987) 109–
982 130.
- 983 [33] M. Renouf, V.-H. Nhu, A. Saulot, F. Massi, First-Body Versus Third-Body: Dialogue Between an
984 Experiment and a Combined Discrete and Finite Element Approach, *ASME J. Tribol.* 136 (2014) 021104.
985 <https://doi.org/10.1115/1.4026062>.
- 986 [34] Y. Berthier, Experimental evidence for friction and wear modelling, *Wear*. 139 (1990) 77–92.
987 [https://doi.org/10.1016/0043-1648\(90\)90210-2](https://doi.org/10.1016/0043-1648(90)90210-2).
- 988 [35] Y. Berthier, Third-Body Reality - Consequences and use of the Third-Body Concept to Solve Friction and
989 Wear Problems, in: *Wear - Mater. Mech. Pract.*, 2005: pp. 291–317.
- 990 [36] G. Colas, A. Saulot, S. Descartes, Y. Michel, Y. Berthier, Double Transfer Experiments To Highlight
991 Design Criterion for Future Self-Lubricating Materials, in: Conf. Proc. 16th Eur. Sp. Mech. Tribol. Symp.,
992 Bilbao, Spain, 2015. <http://esmats.eu/esmatspapers/pastpapers/pdfs/2015/colas.pdf>.
- 993 [37] S. Pajovic, G. Colas, A. Saulot, M. Renouf, T. Filleter, Work of Adhesion Measurements of MoS₂ Dry
994 Lubricated 440C Stainless Steel Tribological Contacts, *Adv. Eng. Mater.* 1700423 (2017) 1700423.
995 <https://doi.org/10.1002/adem.201700423>.
- 996 [38] M.D. Villavicencio, M. Renouf, A. Saulot, Y. Michel, Y. Mahéo, G. Colas, T. Filleter, Y. Berthier, Self-
997 lubricating composite bearings: effect of fiber length on its tribological properties by DEM modelling,

- 998 Tribol. Int. 113 (2017) 362–369. <https://doi.org/10.1016/j.triboint.2016.12.022>.
- 999 [39] S.D. Lewis, M.J. Anderson, A. Haslehurst, Recent developments in performance and life testing of self-
1000 lubricating bearings for long-life applications, in: 12th Eur. Sp. Mech. Tribol. Symp., Liverpool, UK, 2007.
- 1001 [40] C. Cordier, Procedure de nettoyage de pieces mecaniques, metalliques, plastiques, composites ou
1002 ceramiques applique au laboratoire de DCT/TV/MS. DCT-TV-MS-2009-6283-1.0, CNES, 2009.
- 1003 [41] M. Gouider, Y. Berthier, P. Jacquemard, B. Rousseau, S. Bonnamy, H. Estrade-Szwarckopf, Mass
1004 spectrometry during C/C composite friction: Carbon oxidation associated with high friction coefficient
1005 and high wear rate, *Wear*. 256 (2004) 1082–1087. [https://doi.org/10.1016/S0043-1648\(03\)00534-9](https://doi.org/10.1016/S0043-1648(03)00534-9).
- 1006 [42] G. Theiler, T. Gradt, MoS₂ -Filled PEEK Composite as a Self-Lubricating Material for Aerospace
1007 Applications, in: Proc. 40th Aerosp. Mech. Symp., NASA Kennedy Space Center, 2010: pp. 347–352.
1008 <https://ntrs.nasa.gov/archive/nasa/casi.ntrs.nasa.gov/20100021916.pdf>.
- 1009 [43] R. Nevshupa, J. Caro, A. Arratibel, R. Bonet, A. Rusanov, J.R. Ares, E. Roman, Evolution of tribologically
1010 induced chemical and structural degradation in hydrogenated a-C coatings, *Tribol. Int.* 129 (2019) 177–
1011 190. <https://doi.org/10.1016/j.triboint.2018.08.023>.
- 1012 [44] A. Igartua, E. Berriozabal, B. Zabala, F. Pagano, I. Minami, N. Doerr, C. Gabler, R. Nevshupa, E. Roman,
1013 L.P. Nielsen, S. Louring, L. Muntada, W. Neustadt, Lubricity and Tribochemical Reactivity of Advanced
1014 Materials Under High Vacuum, *Proc. 16th Eur. Sp. Mech. Tribol. Symp.* 2015 (2015) 23–25.
- 1015 [45] G. Colas, A. Saulot, N. Bouscharain, C. Godeau, Y. Michel, Y. Berthier, How far does contamination help
1016 dry lubrication efficiency?, *Tribol. Int.* 65 (2013) 177–189. <https://doi.org/10.1016/j.triboint.2012.12.011>.
- 1017 [46] R.A. Nevshupa, J.L. De Segovia, E.A. Deulin, Outgassing of stainless steel during sliding friction in ultra-
1018 high vacuum, *Vacuum*. 53 (1999) 295–298. [https://doi.org/10.1016/S0042-207X\(98\)00366-2](https://doi.org/10.1016/S0042-207X(98)00366-2).
- 1019 [47] D.H. Buckley, R.L. Johnson, Degradation of Polymeric Compositions in Vacuum to 10⁻⁹ mm Hg in
1020 Evaporation and Sliding Friction Experiments, *Polym. Eng. Sci.* 4 (1964) 306–314.
1021 <https://doi.org/10.1002/pen.760040412>.
- 1022 [48] W. Wilkens, O. Kranz, The formation of gases due to the sliding friction of teflon on steel in ultrahigh
1023 vacuum, *Wear*. 15 (1970) 215–227. [https://doi.org/10.1016/0043-1648\(70\)90196-1](https://doi.org/10.1016/0043-1648(70)90196-1).
- 1024 [49] NIST, NIST Chemistry Webbook <https://webbook.nist.gov/chemistry/>, (n.d.). [https://doi.org/DOI:
1025 https://doi.org/10.18434/T4D303](https://doi.org/DOI:https://doi.org/10.18434/T4D303).
- 1026 [50] I.V. Kragelsky, V.V. Alisin, Tribology: Lubrication, Friction and Wear, Tribology, Professional
1027 Engineering Publishing Ltd, Bury St Edmunds, 2005.
- 1028 [51] R.A. Nevshupa, J.L. De Segovia, Outgassing from stainless steel under impact in UHV, *Vacuum*. 64
1029 (2002) 425–430. [https://doi.org/10.1016/S0042-207X\(01\)00345-1](https://doi.org/10.1016/S0042-207X(01)00345-1).
- 1030 [52] G. Colas, A. Saulot, D. Philippon, Y. Berthier, D. Leonard, Time-of-Flight Secondary Ion Mass

- 1031 Spectroscopy investigation of the chemical rearrangement undergone by MoS₂ under tribological
1032 conditions, *Thin Solid Films*. 588 (2015) 67–77. <https://doi.org/10.1016/j.tsf.2015.04.051>.
- 1033 [53] W.O. Winer, Molybdenum disulfide as a lubricant: A review of the fundamental knowledge, *Wear*. 10
1034 (1967) 422–452. [https://doi.org/10.1016/0043-1648\(67\)90187-1](https://doi.org/10.1016/0043-1648(67)90187-1).
- 1035 [54] M. Champagne, M. Renouf, Y. Berthier, Modeling Wear for Heterogeneous Bi-Phasic Materials Using
1036 Discrete Elements Approach, *J. Tribol.* 136 (2014) 021603. <https://doi.org/10.1115/1.4026053>.
- 1037 [55] P.D. Fleischauer, S.V. Didziulis, J.R. Lince, Friction and wear properties of MoS₂ thin film lubricants,
1038 2002.
- 1039 [56] B.A. Krick, J.J. Ewin, G.S. Blackman, C.P. Junk, W. Gregory Sawyer, Environmental dependence of ultra-
1040 low wear behavior of polytetrafluoroethylene (PTFE) and alumina composites suggests tribochemical
1041 mechanisms, *Tribol. Int.* 51 (2012) 42–46. <https://doi.org/10.1016/j.triboint.2012.02.015>.
- 1042 [57] K. Matsumoto, M. Suzuki, Tribological Performance of sputtered MoS₂ films in various environment,
1043 in: *Conf. Proc. 8th Eur. Sp. Mech. Tribol. Symp.*, Toulouse, 1999.
1044 <http://www.esmats.eu/esmatspapers/pastpapers/pdfs/1999/matsumoto.pdf>.
- 1045 [58] M.D. Villavicencio, M. Renouf, A. Saulot, Y. Michel, Y. Mahéo, G. Colas, T. Filleter, Self-Lubricating
1046 Polymer Composites : Using Numerical Tribology To Highlight Their Design Criterion, in: *Conf. Proc.*
1047 *17th Eur. Sp. Mech. Tribol. Symp.*, Hatfield, UK, 2017.
1048 <http://esmats.eu/esmatspapers/pastpapers/pdfs/2017/villavicencio.pdf>.
- 1049 [59] B.A. Krick, A.A. Pitenis, K.L. Harris, C.P. Junk, W.G. Sawyer, S.C. Brown, H.D. Rosenfeld, D.J. Kasprzak,
1050 R.S. Johnson, C.D. Chan, G.S. Blackman, Ultralow wear fluoropolymer composites: Nanoscale
1051 functionality from microscale fillers, *Tribol. Int.* 95 (2016) 245–255.
1052 <https://doi.org/10.1016/j.triboint.2015.10.002>.
- 1053 [60] M. Hässig, K. Altwegg, H. Balsiger, U. Calmonte, A. Jäckel, B. Schläppi, T. Sémon, P. Wurz, J.J. Bertheliet,
1054 J. De Keyser, B. Fiethe, S.A. Fuselier, U. Mall, H. Rème, M. Rubin, Spacecraft outgassing, a largely
1055 underestimated phenomenon, in: *2011 2nd Int. Conf. Sp. Technol.*, 2011: pp. 1–4.
1056 <https://doi.org/10.1109/ICSpT.2011.6064657>.
- 1057 [61] B.D. Green, Satellite Contamination and Materials Outgassing Knowledgebase-An Interactive Database
1058 Reference, *NASA STI/Recon Tech. Rep.* 1 (2001). <https://doi.org/doi:10.2514/6.2001-2957>.
- 1059 [62] E. Robbins, Tribology tests for satellite application: simulation of the space environment, in: *Proceeding*
1060 *1st Eur. Sp. Tribol. Symp.* (ESA SP-111), 1975.

1061



© 2020 by the authors. Submitted for possible open access publication under the terms and conditions of the Creative Commons Attribution (CC BY) license (<http://creativecommons.org/licenses/by/4.0/>).

1062